TECHNISCHE
UNIVERSITÄT
WIEN

Diploma Thesis

Novel Si-based alloying routes for enhancing the oxidation resistance of TiB_x coatings

carried out for the purpose of obtaining the degree Master of Science,
submitted at TU Wien, Faculty of Mechanical and Industrial Engineering,

by

Oskar BECK, BSc

[redacted]

under the supervision of

Ass. Prof. Dipl.-Ing. Dr.techn. Helmut Riedl-Tragenreif
Projektass. Ahmed Adel Ibrahim Bahr, MSc

Institute of Materials Science and Technology - E308-01-2
Applied Surface and Coating Technology

Wien, April 2023

”*Die Neugier steht immer an erster Stelle eines Problems, das gelöst werden will.*”

– Galileo Galilei (1564 – 1641)

The financial support by the Austrian Federal Ministry for Digital and Economic Affairs, the National Foundation for Research, Technology and Development and the Christian Doppler Research Association is gratefully acknowledged (Christian Doppler Laboratory "Surface Engineering of high-performance Components"). We also thank for the financial support of Plansee SE, Plansee Composite Materials GmbH, and Oerlikon Balzers, Oerlikon Surface Solutions AG.

Affidavit:
I declare in lieu of oath, that I wrote this thesis and performed the associated research myself, using only literature cited in this volume. If text passages from sources are used literally, they are marked as such. I confirm that this work is original and has not been submitted elsewhere for any examination, nor is it currently under consideration for a thesis elsewhere. I acknowledge that the submitted work will be checked electronically-technically using suitable and state-of-the-art means (plagiarism detection software). On the one hand, this ensures that the submitted work was prepared according to the high-quality standards within the applicable rules to ensure good scientific practice "Code of Conduct" at the TU Wien. On the other hand, a comparison with other student theses avoids violations of my personal copyright.

Date

Signature

Acknowledgements

I want to thank **Assistant Prof. Dipl.-Ing. Dr.techn. Helmut Riedl-Tragenreif** for the opportunity to write my diploma thesis in his cheerful, sincere and well-led group. Another big thank you for the chance to work on a topic that expands the knowledge of surface coating technology and the sophisticated inputs you give so easily.

Thank you to **Projektass. Ahmed Adel Ibrahim Bahr, MSc**, for letting me work on his project and for the help and supervision throughout the work. Your extensive knowledge, seemingly covering all current research papers, is incredibly motivating. Your challenge to constantly improve the work and the analyses has been very helpful.

Thanks to **Univ.Ass. Dipl.-Ing. Bálint Hajas**, for always being around and ready to help at the Batcave and to **Dipl.-Ing. Werner Artner**, for the help in making sense of messy X-ray diffractograms. Also, thanks to everyone from our group, especially **Anna** and **Sophie**, for the expertise at any given moment.

Thank you for your time, talks, and insights, **Anna, Lena, Sophie, Alex, Emil**, and everyone else in our offices on the 6th floor and from our group. I want to also thank everyone from my studying group, especially **Flo** and **Raphael**, for being around daily. Another round of immense gratitude goes to **Hans, Jan**, and every other off-uni friend of mine. **Áfra**, thank you so much for our shared (uni) path over the last years. It means indescribable much too me.

Mama, Papa: Thank you for offering me the environment which allowed me to conduct my academic studies and made me who I am today.

Contents

List of Figures

List of Tables

List of Equations

List of Symbols & Abbreviations

at. %	atomic percent
BF	bright field
DC	direct current
DCMS	direct current magnetron sputtering
DSC	differential scanning calometry
EDX	energy dispersive X-ray spectroscopy
EEL	electron energy loss spectroscopy
ERDA-RBS	elastic recoil detection analysis-rutherford backscattering
FIB	focused ion beam
hcp	hexagonal close-packed
HIPMS	high-power impulse magnetron sputtering
ICP-MS	inductively coupled plasma-mass spectroscopy
ICP-OES	inductively coupled plasma-optical emission spectroscopy
mol. %	molecular percent
PBR	Pilling Bedworth ratio
RT	room temperature
SAED	selected area electron diffraction
sccm	standard cubic centimetre per minute
SEM	secondary electron microscope
STA, SDTA	simultaneous (differential) thermal analysis
T_r	reference temperature
T_s	sample temperature
TEM	transmission electron microscope
TGA	thermo-gravimetric analysis
TM	transition metal
T_{onset}	oxidation onset temperature
TSR	thermal shock resistance
UHTC	ultra-high-temperature ceramic
XRD	X-ray diffraction

Abstract

Refractory TiB_2 is a promising protective coating material for various applications due to its outstanding thermo-mechanical properties. However, the use of TiB_2 in high-temperature applications is limited by its poor oxidation resistance. This work explores the alloying of $TiB_{2\pm z}$ coatings with secondary $TMSi_2$-based (TM = Ti, Mo) phases and investigates their high-temperature oxidation resistance, phase formation and mechanical properties.

Ternary Ti-Si-$B_{2\pm z}$ and quaternary Ti-Mo-Si-$B_{2\pm z}$ coatings were sputter-deposited from alloyed TiB_2/$TMSi_2$ target materials using two different power modes of DCMS and HIPIMS. All as-deposited alloyed coatings exhibit the single hexagonal AlB_2-structured phase. Moreover, the coatings' mechanical properties (hardness and elastic modulus) decrease with the increase in alloying content (Si, Mo).

Regarding their oxidation behaviour up to 1400 °C, the quaternary Ti-Mo-Si-$B_{2\pm z}$ coatings outperform their ternary counterparts by preserving outstanding oxidation resistance with delayed oxidation kinetics up to ∼1340 °C due to the formation of a protective Si-based oxide scale. The $Ti_{0.23}Mo_{0.07}Si_{0.17}B_{0.53}$ coating shows retarded oxidation kinetics up to 60 h at 1200 °C by forming a thin protective dense SiO_2 oxide scale (thickness ∼1 µm), which inhibits inward oxygen diffusion. The high-temperature oxidation resistance of Ti-Mo-Si-$B_{2\pm z}$ coatings is attributed to the formation of a separate $MoSi_2$ phase (at $T > 650$ °C, determined by in-situ XRD analysis and TEM investigation) facilitating the supply of Si to form a protective SiO_2 based scale and suppresses the formation of volatile B_2O_3.

Kurzfassung

Dank seiner hervorragenden thermo-mechanischen Eigenschaften ist refraktäres TiB_2 ein vielversprechendes Beschichtungsmaterial für diverse Anwendungsgebiete. Allerdings limitiert die begrenzte Oxidationsbeständigkeit eine breite Anwendungen erheblich. In dieser Arbeit werden Schichten aus $TiB_{2\pm z}$ mit $TMSi_2$ (TM = Ti, Mo) basierten Legierungen auf die sich bildenden Phasen und mechanischen Eigenschaften untersucht.

Die ternären und quaternären Ti(-Mo)-Si-$B_{2\pm z}$ Schichten wurden aus legierten TiB_2/$TMSi_2$ Target-Materialien mittels physikalischer Gasphasenabscheidung (PVD) abgeschieden, wobei zwei verschiedene Sputter-Techniken zum Einsatz kamen (DCMS und HIPIMS). Die erzeugten Schichten konnten alle in der hexagonalen AlB_2 Struktur stabilisiert werden. Das Zulegieren von Mo und Si verringert die mechanischen Eigenschaften in Form von Härte und Elastizitätsmodul.

Bei der Oxidationsbeständigkeit bis zu 1400 °C waren die quaternären Ti-Mo-Si-$B_{2\pm z}$ den ternären Schichten deutlich überlegen. Sie wiesen, dank einer sich bildenden, schützenden Si-basierten Oxidschicht, eine reduzierte Oxidationsrate bis zu ~1340 °C auf. Die rasche Ausbildung der dünnen, dichten und schützenden SiO_2 Schicht mit einer Dicke von ~1 µm ermöglicht der $Ti_{0.23}Mo_{0.07}Si_{0.17}B_{0.53}$ Schicht ein außergewöhnlich gutes Oxidationsverhalten bis zu 60 Stunden bei 1200 °C. Dies ist möglich, da SiO_2 die Sauerstoffdiffusion in Richtung unversehrtes Schichtmaterial verhindert. Die Bildung von $MoSi_2$ aus der hexagonalen $TiB_{2\pm z}$ Einzelphase über 650 °C begünstigt das Entstehen der SiO_2 Schutzschicht, durch eine verstärkte Versorgung mit Si. Gleichzeitig wird die Bildung des volatilen Oxids B_2O_3 unterdrückt.

Chapter 1

Introduction

Over time most metals transform into their chemically stable oxidised form. In this state, they can be found in nature [1]. The destructive oxidation process in high-temperature ambient atmospheres is called dry corrosion [2], which is the abrasion of materials through contact with reactive agents [3, 4]. Ultimately, the materials lose their desired mechanical properties [2], can no longer withstand occurring forces in their application, and need a replacement. In 2013, the cost of corrosion was USD 2.5 trillion, which transferred to 3.4 % of the global GDP, excluding fees for safety and environmental measures [5]. Therefore, it is of great interest to reduce the corrosion rate of metals. Although, the oxidation cannot be stopped altogether [4, 5].

High temperatures elevate the oxidation rate of materials [1, 2]. Therefore, materials exposed in such environments must be highly oxidation resistant while maintaining the desired mechanical properties. An example of a high-performance application is turbine engine components: the currently applied Nickel-based superalloys can withstand high forces at high temperatures [2, 6]. However, their parabolic oxidation rate increases significantly above 850 °C [6–8], and the oxide layers peel off due to a mismatch of internal stresses [8].

Applying surface protective coatings can solve this issue by decreasing the oxidation kinetics [2]. Among the possible manufacturing strategies for protective coatings is physical vapour deposition (PVD) [9], wherein magnetron sputtering has been applied in this work to synthesise TiB_x-thin films alloyed with Si-based secondary phases.

Transition metal diborides (TMB_2) from subgroups 4-6 stand out with good thermo-mechanical properties, chemical stability, and electrical conductivity [10–12]. In particular, bulk-TiB_2 has an extremely high melting point of 3225 °C and a high hardness of 25 – 35 GPa [11]. For sputter-deposited thin films, Mayrhofer et al. [13] reported TiB_2 crystallising in the hexagonal C32 structure with an outstanding hardness of 48 – 77 GPa. A $TiB_{2.4}$ coating developed the highest hardness of 77 GPa [14]. These hardness values offer

TiB_2-coatings to be suitable for the most demanding applications [13].

Cai et al. [15] reported that the oxidation in bulk-TiB_2 between 400 °C and 650 °C proceeds rapidly due to an amorphous Ti-B-O sublayer losing its protective abilities in this temperature range. A protective oxide scale builds up in the temperature range of 650 °C to 1000 °C in the form of TiO_2 and a glassy B_2O_3 layer. Over 1000 °C, the B_2O_3 quickly evaporates, leaving a porous TiO_2 skeleton with accelerated oxidation kinetics [16, 17]. However, the oxidation behaviour of TiB_2-coatings differs significantly from its bulk counterpart: The onset oxidation temperature is around 300 °C, from which point the thin film oxidises with a linear kinetic. [12, 18, 19]

Alloying strategies based on the addition of secondary phases can improve the oxidation resistance of TiB_2 significantly [19]. According to the Ellingham-Richardson diagram, silicon is a feasible alloying element as its oxides' stability exhibits low standard free energy and a high melting point [20]. Fahrenholtz et al. [21] name the following components for Si-alloying routes that have been explored with bulk-TiB_2: $TiSi_2$, $MoSi_2$, SiC, Si_3N_4, WSi, and $CrSi_2$ [21]; Taking Si-alloying paths has successfully improved the oxidation resistance by developing an amorphous borosilicate oxide layer on top for TMB_2, including TiB_2, at temperatures above 1000 °C [22, 23]. Moreover, alloying bulk-TiB_2 with SiC increases the hardness while the toughness decreases significantly [24]. Bulk-TiB_2 alloyed with $TiSi_2$, and $MoSi_2$ phases develop high hardness values sustained in high-temperature environments [21, 25–27].

Glechner et al. [28] applied the Si-alloy strategy in TMB_{2z} (TM = Ti, Cr, Hf, Ta, W) thin films achieving a glassy Si-based protective oxide scale formation for Ti, Hf, and Cr, which withstands temperatures above 1200 °C. However, the silicon content significantly reduced the hardness of TiB_2 coatings [28]. Grančič et al. [29] slightly enhanced the hardness of Ti-Si-B thin films through high-temperature vacuum annealing. Upon annealing, the Si-rich amorphous material fraction reduced within the coating, and TiB_2 crystals grew distinctly [29].

In this work, the author applies the promising alloying route for TiB_x coatings based on $TMSi_2$ phases (TM = Ti, Mo), which has proven successful for bulk-TiB_2. The alloyed Ti(-Mo)-Si-$B_{2\pm z}$ coatings are synthesised by direct current magnetron sputtering (DCMS) and high-power impulse magnetron sputtering (HIPIMS) from alloyed $TiB_2/TMSi_2$ targets with varied compositions. Afterwards, dynamic and isothermal oxidation tests were carried out to investigate the oxidation behaviour in relation to the phase formation and mechanical properties of all alloyed Ti(-Mo)-Si-$B_{2\pm z}$ coatings. The main goal is to find the optimum alloying concept for TiB_x coatings, in which the high-temperature oxidation resistance improves while good mechanical properties are maintained.

The material system and the deposition process are the content of Chapter 2. Thereby it forms the theoretical foundation of this work. In the following Chapter (3), the author describes the methods of analysis. The experimental details are presented in Chapter 4. Afterwards, the author renders the results and discussions in Chapter 5. This section is the most relevant as it will depict the learnings of the whole work. Chapter 6 contains the conclusions.

Chapter 2

Literature review

2.1 Titanium diboride

Transition metals from subgroups 4-6 paired with boron (TMB) experience a very high melting point, excellent thermal and chemical stability, and high hardness. Hence, they are within the Ultra-High Temperature Ceramics (UHTC) group, with a melting point above 3000 °C. TMBs get their properties from mixed covalent, ionic, and metallic atomic bonds [10–12]. Fahrenholtz et al. [21, 30] and Magnuson et al. [12] thoroughly described how chemical bonding and composition influence the overall material's characteristics. The ratio between metal (Me) and boron (B) affects the whole system and, therefore, the impact of individual bonds within a material system as each bonding type changes different features. The TMB_x formula reflects this ratio, which generally varies from 4:1 to 1:12 (TM:B). [12, 21, 30, 31]

Binary phase diagrams like in Figure 2.1 depict which intermetallic phases form for a specific TMB. In this work, the Ti-B system is the system of interest, developing two orthorhombic phases (TiB, Ti_3B_4) and a hexagonal phase (TiB_2, marked in blue in Figure 2.1). All these phases have a narrow stoichiometry in which they form [21]. Within the starting temperature of 500 °C, the stoichiometry of the developing hexagonal TiB_2-film can vary slightly [12]. This phase is the most interesting as it has a UHTC-compliant melting point of 3225 °C [21] and crystallises in the typical hexagonal close-packed AlB_2 C32 crystal structure with space group p6/mmm (space group number 191) [10–12, 21, 30, 32].

The crystal structure of the AlB_2-type has a stacking sequence consisting of an alternating ABABAB-order (Figure 2.2b): Ti takes the A-place with six equidistant Ti neighbours in each A-plane assembling in an AAA sub-order while B fills the interstitial B-plane. Six B-atoms per plane are in equidistance to a Ti-atom. A and B planes are hexagons strung into nets (Figure 2.2a) [11, 12, 21, 30, 31, 33]. The covalent B-B bonds control the melting temperature, hardness, strength, and chemical stability. Ti-B bonds have a minor influence on

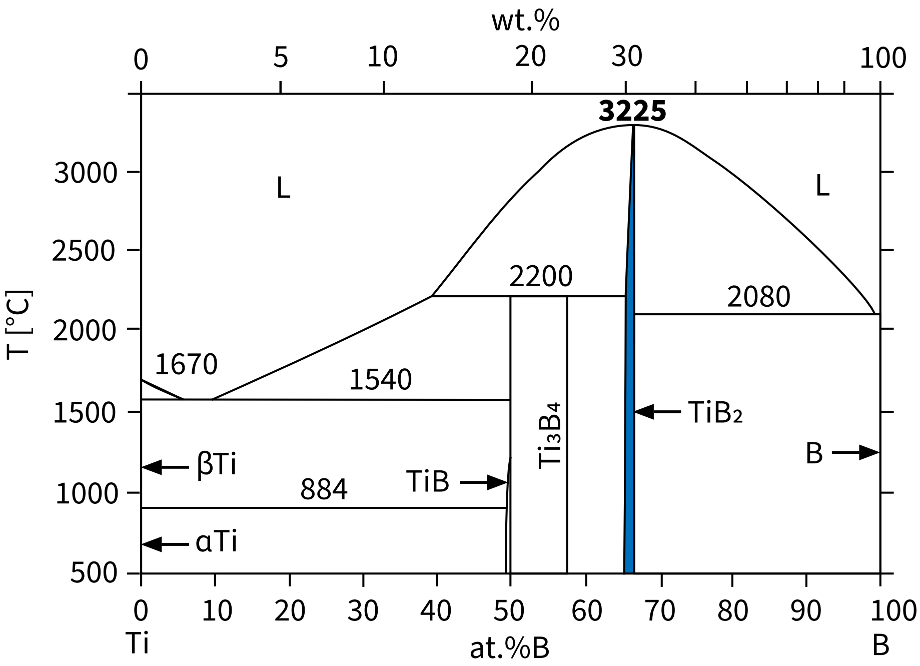

Figure 2.1: Binary phase diagram Ti-B (adapted from [21]).

the a-axis length beside the B-B bonds. The hcp-structure (hexagonal close-packed structure) leads to anisotropy within a single crystal: The Ti-atom is at (0,0,0), and the interstitial B-atom is at (1/2,2/3,1/2) and (2/3,1/3,1/2) respectively. The angles in the unit cell are $\alpha = \beta = 90°$ and $\gamma = 120°$ [11, 21, 30, 33].

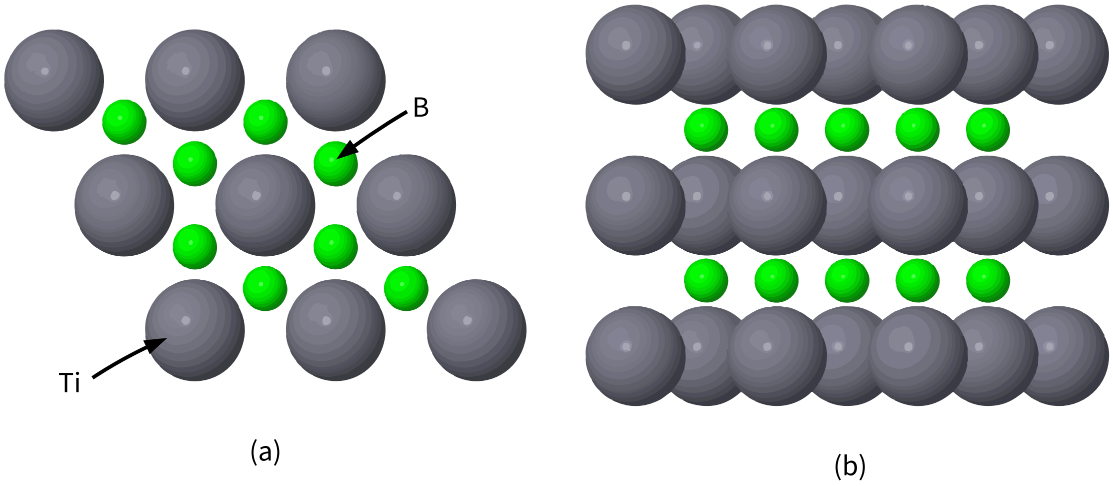

(a)

(b)

Figure 2.2: Crystal structure (a) and stacking order (b) TiB_2 (adapted from [34]).

The reported properties of TiB_2 differ depending on the material being polycrystalline or a single crystal, bulk material, or a thin film, as well as the purity and the production method with resulting different morphology and density [35]. Polycrystalline bulk-TiB_2 develops isotropic properties due to the statistical orientation of the anisotropic single crystals. The single crystal's hardness is angle-dependent varying up to 30 % [36]. Fahrenholtz et al. [21], Goh et al. [33], and Golla et al. [11] compared data collected from the literature on polycrystalline bulk-TiB_2 to other transition metal diborides' properties and reported the following differences formulated for the TiB_2's properties: Low-density, high thermal conductivity, high linear thermal expansion, high elastic modulus, high hardness, and high flexural strength; Even though the fracture toughness is in line with other transition metal diborides and other covalently bonded ceramics, it is low compared to other materials such as steels [11, 32, 37].

For TiB_2 to be a UHTC, mechanical properties and chemical stability must persist at elevated temperatures, wherein ceramics as bulk-TiB_2 lose hardness with increasing temperature in an exponential relation [11, 21]. The hardness of monolithic bulk-TiB_2 drops from ~25 GPa at room temperature (RT) to under 5 GPa at 1000 °C [35], and the hot elastic modulus decreases from ~565 GPa at RT to 510-534 GPa at 1000 °C [11, 21, 35], while the high-temperature strength increases at this temperature. Exact values depend heavily on the source, but the increase is within the range of 59 MPa to 100 MPa starting from about 300 MPa. [11, 33, 35] The thermal shock resistance (TSR) of TMB_2 is generally considered good due to their high strength and high thermal conductivity [11].

These favourable properties of bulk-TiB_2 led to the investigation of TiB_2 thin films [38]. The same AlB_2 hexagonal structure forms within sputtered thin films compared to bulk-TiB_2 [38, 39]. DC magnetron-sputtered TiB_2 thin films form in a mainly homogenous columnar pattern along the 0001 orientation [39–41]. According to Mayrhofer et al. [13], the exceptional hardness observed in overstoichiometric $TiB_{2.4}$ thin films originates from two effects: The formation of nanocolumnar structured TiB_2 with subcolumns that are only about $\frac{1}{4}$ of the columns' average length, which makes dislocation formation difficult. Additionally, the B-rich tissue phase building at the grain boundaries (Figure 2.3) hinders the dislocation motions and enhances the cohesive strength of the thin film. However, the material behaves as anisotropic, which displays through the relative intensity fraction of the 0001 peaks in the X-ray diffraction (XRD) diagram. [13] With increasing anisotropy, the hardness of TiB_2 can increase: The hardness depends on the fraction of {0001} oriented grains, from <10 % to >99 %, exhibiting values from ~27 GPa to ~41 GPa. Additionally, the smaller crystallite sizes decrease hardness from ~41 GPa to ~34 GPa. [40] This simultaneous decrease of hardness and grain size derives from the 'reverse Hall-Petch effect' [38]: From a specific grain size going smaller, dislocations rely on the broadly available grain boundaries for sliding when confronted with an external force [42, 43].

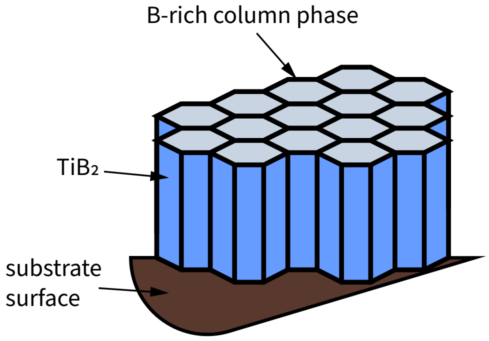

Figure 2.3: TiB_2 columns with B-rich boundaries (adapted from [44]).

Stoichiometry plays a vital role in the resulting properties of TiB_2 coatings and varies when altering deposition parameters during non-reactive direct current (DC) sputtering [38, 45]. A change in B-content in TiB_2 thin films affects the properties decisively [40] while retaining the hexagonal structure [38]. A higher B content leads to increased crystal lattice parameters, higher density, smaller grain size, and increased hardness from the stoichiometric value of ∼38 GPa to ∼52 GPa for $TiB_{2.23}$ [38]. However, Thörnberg et al. [45] also achieved an increase in hardness from ∼41 GPa to ∼43.9 GPa for understoichiometric TiB_2 films. The high hardness predicates upon the understoichiometric film's finer columns compared to the stoichiometric TiB_2 ones and planar defects within the B-deficient columns. The elastic modulus decreased from ∼541.8 GPa to ∼511 GPa. [45, 46]
In general, TiB_2 coatings are brittle and under high internal stress after deposition. Sputtering with reduced or positive bias voltage [39, 47] or vacuum annealing [48] can relieve some stress and retain the mechanical properties and the chemical composition [38, 39].

2.1.1 Oxidation

High temperature accelerates corrosion processes like the reduction-oxidation (redox) reaction exponentially. This reaction occurs between gaseous oxygen (O_2) and metals (Me) and consists of two parts: Firstly, the scale adsorbs O_2 into the material's surface, reducing it to O^{-2} by accepting electrons (e^-). Secondly, on the other side of the scale, a metal atom diffuses from the metal alloy into the scale and oxidises by releasing the needed e^- and creating a positively charged Me^+. Finally, O^{-2} and Me^+ form the oxide where the correct ratio xMe:$\frac{y}{2}O_2$ is indispensable and depends on the involved metal. The following formula summarises the whole redox process sketched in Figure 2.4: [2, 49]

$$\frac{x}{y}Me + \frac{1}{2}O_2 \rightarrow \frac{1}{y}Me_xO_y \text{ with } x, y \in \mathbb{N} \tag{2.1}$$

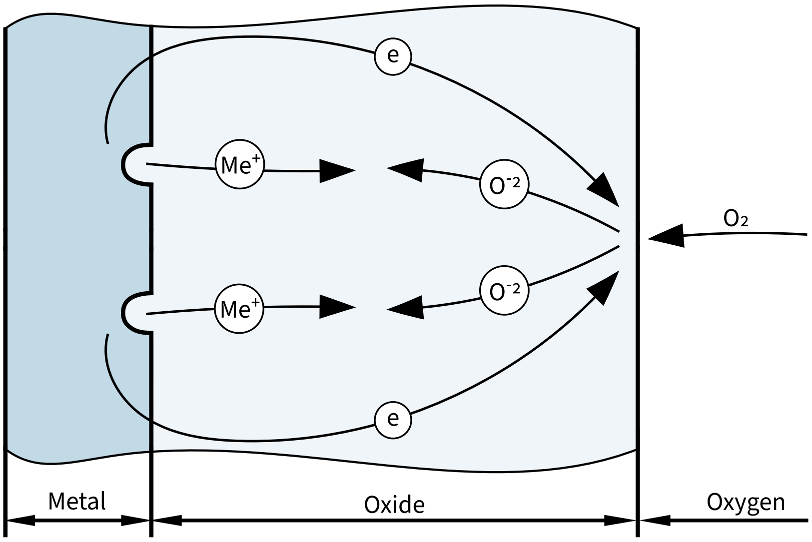

Figure 2.4: Schematic illustration of the redox reaction (adapted from [49]).

The redox reaction varies in speed depending on the place within the scale [2]. Among others, the statistical adsorption when building a new scale and the diffusibility of cations and oxygen ions are responsible for this behaviour [49, 50]. Diffusion also determines the place of the scale growth, which can either happen at the metal-scale or the scale-atmosphere interface [49].

Diffusion as the primary driver of oxidation allows the kinetic theory to describe the oxidation progress over time t. Researchers empirically observed and formulated oxidation rates for different behaviours assuming an ideal, adherent oxide scale in thermodynamic equilibrium. [49–51] The following formulas calculate the accumulated mass gain over area W with time. However, depending on the source, one may substitute the mass gain with the scale thickness within the same mathematical expressions.

The linear oxidation relationship formulates as follows:

$$W = k_l t \tag{2.2}$$

Where k_l is the linear rate constant [49]. The linear oxidation behaviour develops when oxidation at the phase boundary is the determining factor. It occurs at the initial stages of the redox reaction when the oxide scale is too thin to make the diffusion rate relevant [50]. If the oxidation kinetics remain at this rate, the formed scale is porous or cracked, which makes the layer non-coherent and lets the oxygen directly reach the metal-scale interface. Pure Ti oxidises linearly due to this phenomenon. A volatile scale formation has the same behaviour while exhibiting a negative slope. [49, 51]

The parabolic rate oxidation reflects the ideal diffusion-controlled behaviour:

$$W^2 = k_p t + C \tag{2.3}$$

Where k_p being the parabolic rate constant and C being an occurring constant. The rate derives from Fick's first law assuming a steadily growing layer driven by a constant diffusion coefficient [49, 51].

Among other expressions, the logarithmic oxidation rate formulates as this:

$$W = k_e log(Ct + A) \tag{2.4}$$

k_e, C and A are constants. This behaviour occurs in thin oxide layers at temperatures up to 400 °C [49]. Most likely, the logarithmic oxidation develops from a mixture of effects from quantum mechanical tunnelling of electrons within the scale, blocking of low-resistance diffusion paths, local non-isothermal conditions, local stoichiometry, and others. [50]

In some experiments, another oxidation rate occurred. It has been named the cubic oxidation rate:

$$W^3 = k_c t + C \tag{2.5}$$

k_c, C are constants. The cubic rate occurs due to a superposition of different effects rather than a novel mechanism. [49] In general, other oxidation rates can develop based on a mixture of the above-described rates and other factors [50].

Figure 2.5 visualises the oxidation rates described above. All rates intersect at one point to make the growth ratios comparable. However, the constants can vary remarkably, and the observable oxidation rates may differ significantly from this Figure. [51]

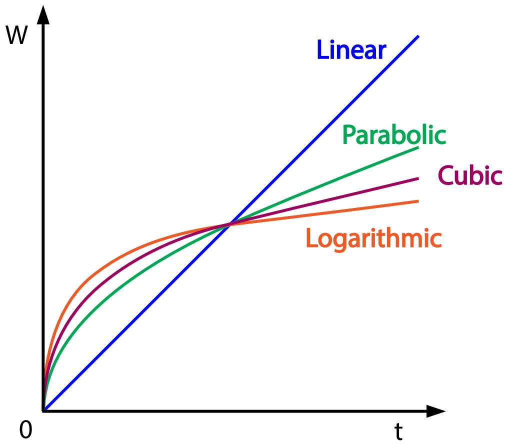

Figure 2.5: Oxidation rates (adapted from [49]).

The linear oxidation growth depends on a mechanism described by Pilling and Bedworth. They figured that the volumetric coherence of the scale influences the oxidation resistance. The qualitative relation derives from the volume ratio of oxide (V_{oxide}) and metal (V_{metal}):

$$PBR = \frac{V_{oxide}}{n \cdot V_{metal}} \tag{2.6}$$

Ratios of PBR<1 and PBR>2 indicate an insufficient oxidation resistance due to stresses originating in the volumetric misfit. These compressive and tensile stresses lead to cracking and, in the latter case, scale spallation. Hence, ratios slightly above 1 or 1 are favourable as no significant volumetric misfit establishes. Contradicting observations to this theory occur due to other equally influencing properties such as non-fitting expansion coefficients, adherence, melting points, fracture toughness, et cetera. [49]

Oxidation of bulk-TiB_2

The primary stable oxidation process of bulk TiB_2 above 600 °C sums up to: [52, 53]

$$TiB_2(s) + \frac{5}{2}O_2(g) \rightarrow TiO_2 + B_2O_3(l/g) \tag{2.7}$$

s, g and l stand for the states of matter: solid, gaseous, and liquid. Additionally, according to the Ti-B-O diagram, Ti_3O_5 forms a stable oxide if there is an oxygen deficit in the reaction [54].

However, the oxidation process appears more complex in detail: TiB_2 starts to oxidise around 100 °C until 400 °C in a reversible process reflected in the formula beneath: [21, 55]

$$4TiB_2 + 9O_2(g) \rightarrow 4TiBO_3 + 2B_2O_3 \text{ and } 0.05 \text{ ppm } O_2 \tag{2.8}$$

At 400 °C, Tampieri et al. [52] detected cracks and bubbles in the surface. Cai et al. [15] reported the formation of an amorphous Ti-B-O layer at about 400 °C. At 500 °C, the oxide comprises an outer amorphous B_2O_3/TiO_2 layer and an inner amorphous Ti-B-O scale. The latter is an unstable inner sublayer that experiences reduced viscosity, leading to accelerated oxygen diffusion compared to the diffusivity at 400 °C and 600 °C. Simultaneously, the formation of anatase TiO_2 leads to the cracking of the oxide scale as it expands its volume with the rapid scale growth. [15] In other literature reviewed by the author, a stable, protective oxide scale develops in the temperature range of 400 °C to about 850 °C: An inner TiO_2 layer forms with a protective, liquid amorphous B_2O_3 layer on top completing the primary oxidation reaction: [17, 21, 55]

$$4TiBO_3 + O_2 \rightarrow 4TiO_2 + 2B_2O_3 \text{ and } 10 \text{ ppm } O_2 \tag{2.9}$$

In the range of 700 °C to 850 °C, a diffusion-controlled, parabolic oxidation rate develops with a very protective, pliable B_2O_3 layer [17, 22, 52, 53, 56, 57]. Only at this temperature is crystalline B_2O_3 detected, as it already starts to dissolve at 800 °C [52, 55]. Tampieri et al. [52] observed a parabolic oxidation rate up to the considerably higher temperature of 1100 °C for 500 min, while Barandika et al. [58] reported a change in the oxidation behaviour already at 750 °C for TiB_2 cermet due to metallic binders. At 900 °C, the liquid B_2O_3 protective scale evaporates almost instantly and a highly textured TiO_2 surface establishes: [52, 53, 56, 57]

$$B_2O_3(l) \rightarrow B_2O_3(g) \tag{2.10}$$

The textured surface, accompanied by a thermal expansion mismatch between the bulk-TiB_2 and the TiO_2 surface layer, leads to pores and cracks. Consequently, rapid oxidation happens. Based on gravimetric measured experiments for oxide growth, the literature data identifies the kinetics between 900 °C and 1000 °C, the main range for B_2O_3 evaporation, as linear [21, 58–60]. In contrast, earlier studies have identified the oxidation rate to follow the cubic rate when measuring volumetric oxidation changes [53, 56, 57].

Above 1200 °C, the B_2O_3 oxide evaporates instantly. The evaporation of B_2O_3 leads to a highly textured and thick, crystalline rutile TiO_2-phase, which develops a parabolic oxidation rate: [17, 52, 53, 56, 57]

$$TiB_2(s) + \frac{5}{2}O_2(g) \rightarrow TiO_2(s) + B_2O_3(g) \tag{2.11}$$

Oxidation of TiB_2 thin films

For TiB_2 thin films, the observed oxidation behaviour differs from the bulk materials. The evaporation of B_2O_3 in thin films starts at 140 °C due to a reaction with water vapour in ambient air. The reaction completes at about 400 °C leaving gaps where the B had been. [19, 41, 61, 62] This effect develops more pronounced for overstoichiometric $TiB_{2\pm z}$ due to the boron concentrated at the grain boundaries (Figure 2.3), which rapidly evaporates upon oxidation, resulting in void formation. Through these voids, oxygen gas enters to reach and react with a highly enlarged TiB_2 surface area, as seen in Figure 2.6. The porous scale oxidises rapidly at a linear rate from 300 °C to 500 °C. [19, 40, 41, 63] The resulting oxide scales can be seen in Figure 2.7.

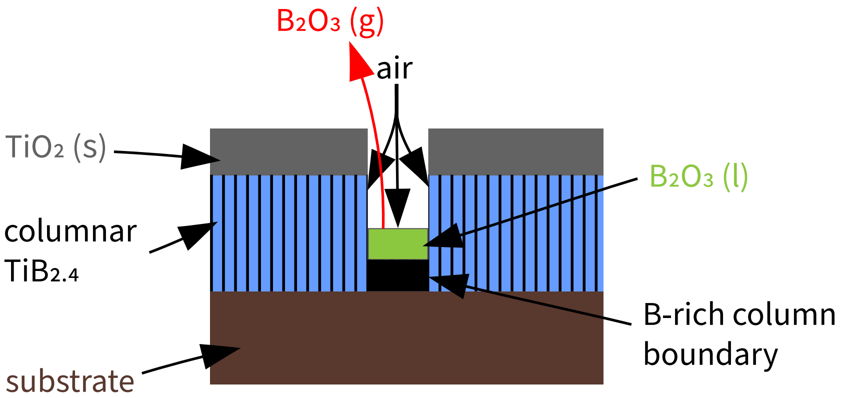

Figure 2.6: Schematic illustration of $TiB_{2.4}$ at 700 °C during the oxidation (adapted from [63])

Over 500 °C, the main phase in the oxide scale is homogenous, crystalline, rutile TiO_2 [19, 41, 63]. There is a distinct B deficiency. Dorri et al. [19] recorded a linear oxidation rate for $TiB_{2.5}$ thin films between 500 °C and 700 °C. However, they identified an abnormally low, parabolic, and protective oxidation rate at 600 °C compared to those at 500 °C and 700 °C (Figure 2.7). At 600 °C, the oxide scale consisted of a highly dense TiO_2 layer embedded in an amorphous Ti-B-O layer, acting as an oxygen diffusion retardant. [19] After 0.5 h at 800 °C, Bakhit et al. [63] observed that their 1.9 µm $TiB_{2.4}$ layer was completely oxidised.

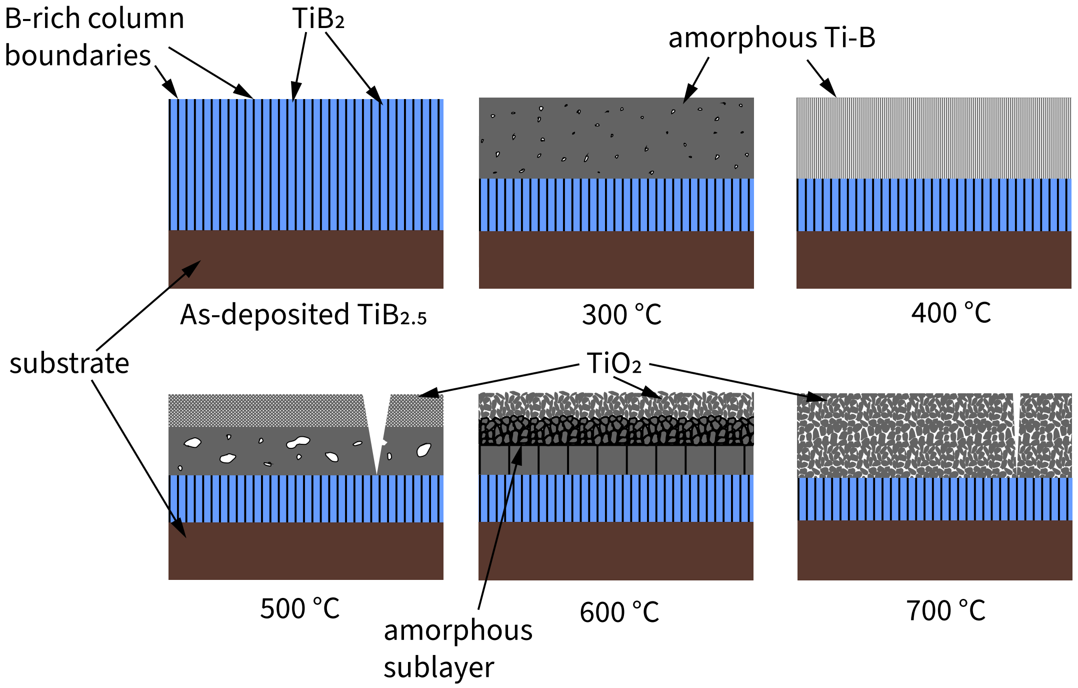

Figure 2.7: Illustrated cross-sections of an air-annealed $TiB_{2.5}$ layer at temperatures written beneath the respective sketch (adapted from [19]).

Regarding the stoichiometry of the sputtered $TiB_{2\pm z}$ films, the oxide scales of B-rich $TiB_{2\pm z}$ films grow faster and less dense than the B-deficient ones: Boron under-stoichiometric $TiB_{2\pm z}$ showed oxidation resistance at 400 °C for up to 48 h, with reported oxidation rates of: 2.9 ±1.5 nm/h for $TiB_{1.43}$, compared to 7.1 ±1.0 nm/h for $TiB_{2.2}$, and 20.0 ±5.0 nm/h for $TiB_{2.7}$ [41].

2.1.2 Silicon alloying of $TiB_{2\pm z}$

The goal of alloying TMBs is to improve their high-temperature oxidation resistance while retaining a similar level to the other material properties. Nevertheless, hardness and elastic modulus will decrease inevitably upon alloying with elements improving the oxidation resistance, such as Al and Si. A tertiary alloying element should oxidise after the least noble of the binary base material system to be capable of building a protective oxide layer. Furthermore, the additional component must be soluble in the primary MeO_x layer to diffuse through and form a second oxide scale on top, which acts as a diffusion barrier for metals and oxides. [51]

An alternative promising alloying route to the one applied in this work is $TiB_{2\pm z}$ thin films alloyed with Al. They exhibit a significantly improved oxidation resistance up to 800 °C, presenting an oxidation onset temperature of 600 °C. Responsible for the enhancement is the high oxygen affinity of Al concentrated at the grain boundaries of $TiAlB_{2\pm z}$ to form Al_2O_3 oxide upon oxidation. This behaviour hinders the coarsening of TiO_2 columns making the scale's inner layer dense, while the outer oxide layer exhibits some porosity. [18, 63] However, the hardness of the Al-alloyed films dropped significantly compared to binary $TiB_{2\pm z}$: Navidi Kashani et al. [18] achieved excellent oxidation resistance up to 700 °C paired with a maximum hardness of ∼25 GPa (decreased from ∼38 GPa [28] for binary $TiB_{2\pm z}$ thin films) for an over stoichiometric $(Ti_{0.34}Al_{0.66})B_{2.4}$ film. They reported an elastic modulus of ∼330 GPa [18] (decreased from over 500 GPa [45, 46]). Bakhit et al. [63] retained a very high hardness (∼39 GPa) with $Ti_{0.68}Al_{0.32}B_{1.35}$ thin film while improving the oxidation resistance to a lesser degree than Navidi Kashani et al. [18] with their thin films.

Opeka et al. [64] concluded in their literature review that the primary, stable oxide based on silicon, SiO_2, develops superior high-temperature capabilities. SiO_2 exhibits a melting temperature of 1865 °C in ambient pressure and a more pronounced structural tolerance than other oxides due to its glassy, amorphous character where oxidation products, such as SiO, can diffuse outwards through the scale without breaking the SiO_2 protective property. This way, the interfacial (metal) vapour pressure that increases with temperature from the inner regions of the coating cannot disrupt the scale. On the contrary, Cr_2O_3, Al_2O_3, and BeO are crystalline oxides that allow only internal ionic diffusion, making them vulnerable to interfacial vapour pressures. [64]

Si and TiB_2 are thermodynamically compatible due to similar thermal expansion coefficients allowing for low stresses [65, 66]. To date, researchers tested most Si-alloying approaches for bulk composites. However, no quantitative data are given in this section as they are highly dependent on the manufacturing technology and the resulting bulk density. Therefore, the author makes qualitative statements to provide an overview of the results: SiC-TiB_2-Al-Si bulk composite forms a protective, Al-B-Si-rich oxide scale enabling parabolic oxidation kinetics [67]. Bulk SiC-TiB_2 in various compositions exhibits increased RT hardness and a further loss in fracture toughness compared to monolithic TiB_2. Unfortunately, no oxidation tests have been reported. [24] TiB_2 alloying routes with $CrSi_2$ and WSi_2 in the bulk system led to a modest decrease in hardness and a decline in fracture toughness combined with reported low parabolic oxidation kinetics at 850 °C with increasing alloying content [68, 69]. For TiB_2-Si_3N_4 bulk composites, a protective, borosilicate layer retards the oxidation rate above 1000 °C until ∼1250 °C while decreasing fracture toughness and hardness moderately [70, 71].

Regarding Si-alloyed coatings, a SiC-TiB_2 sprayed coating in the ratio 1.5:1 developed a protective borosilicate layer at 700 °C in ambient air [72]. With the deposition of TM-Si-B (TM = Ti, Cr, Ta, Hf, W) thin film systems, Glechner et al. [28] successfully applied the Si-alloying route for PVD sputtered coatings. Also, Grančič et al. [29] alloyed $TiB_{2\pm z}$ coatings with Si. Recorded in both investigations, the alloying of Si decreased the hardness of $TiB_{2\pm z}$ thin films from ∼38 GPa to ∼22 GPa at 20 at. % Si [28] and the elastic modulus from over 500 GPa [45, 46] to ∼175 GPa at 10 at.% Si [29]. By annealing the coatings at 800 °C for 1 h, Grančič et al. [29] hardened their TiB_2 thin film with 10 at. % Si content from ∼17 GPa to ∼28 GPa and increased the elastic modulus from ∼175 GPa to ∼230 GPa. During (air-)annealing, the amorphous Ti-Si-B thin films crystallise further and develop distinct Si peaks. No Si peaks appear in the XRD spectra of the as-deposited coatings, contrasting with comparable bulk systems that develop separate, Si-based phases. [28, 29] The morphology of as-deposited Ti-Si-$B_{2\pm z}$ is similar to pure $TiB_{2\pm z}$ thin films but forms finer crystalline columnar grains. However, the intensity peaks in the XRD spectra grow broader with increasing Si content [29].

The oxidation of the Ti-Si-$B_{2\pm z}$ thin film system occurs slower with increasing Si content. [29] As reported by Grančič et al., above 500 °C in ambient air, the coating surface appeared shiny, without cracks, but with decreased B content. They also exhibited an increase of Si compared to Ti, which may originate from the outward diffusion of silicon. The formed oxides at 500 °C are anatase TiO_2 and B_2O_3. [29] At 900 °C for 1 h in synthetic air, Glechner et al. [28] reported phases of rutile TiO_2, TiB_2, and elemental Si. After 1 h at 1100 °C, distinct peaks of TiB_2, Si, and a minor rutile TiO_2 peak (not visible in the taken SEM cross-sections) matured (Figure 2.8). At this temperature, the coating had developed a highly protective, amorphous Si-rich borosilicate layer on top. [28] Grančič et al. [29] obtained similar results in their 10 at. % Si coating annealed in ambient air at 800 °C: A protective, amorphous borosilicate-rich top layer and a mostly rutile TiO_2 sublayer. Conversely, they detected another glassy borosilicate layer underneath these layers and another rutile TiO_2 layer under which the remaining unoxidised coating was located. The alternating layer arrangement may have resulted from a reaction between water vapour and boron [29]. The synthetic air used in Glechner et al.'s [28] setup eliminated the chemical response and achieved an oxidation onset temperature of 490 °C for $TiB_{2.72}$.

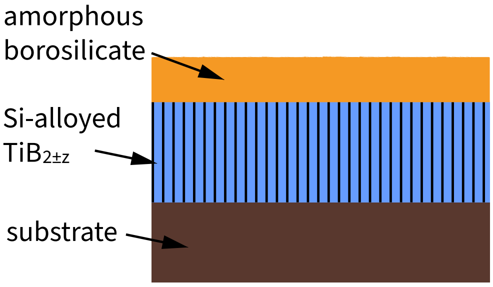

Figure 2.8: 1 h isothermal oxidation in synthetic air at 1100 °C of a Ti-Si-B thin film

$MoSi_2$-based alloying route for $TiB_{2\pm z}$

Since the 1950s, $MoSi_2$ has been used for heating elements in high-temperature furnaces due to its excellent oxidation resistance. However, the composite experiences the 'pesting phenomenon' in the temperature range from 400 °C to 600 °C: Porosity, in addition to internal and external stresses, lead to cracks, where oxygen enters. The building oxide product MoO_3 advances through these cracks by wedge-loading. Below 750 °C, the oxidation products are MoO_3 and SiO_2, whereas, above this temperature, Mo_5Si_3 and SiO_2 develop while MoO_3 evaporates quickly. The oxygen diffusion controls the oxidation kinetics through the glassy, protective SiO_2 top layer. Therefore, they are parabolic. [73–75]

In bulk $MoSi_2$ alloyed with 30 vol. % TiB_2, a semi-protective glassy B_2O_3 layer starts forming at around 500 °C, suppressing the 'pesting phenomenon' [73]. Cook et al. [73] observed no cracking and pesting in their bulk TiB_2-$MoSi_2$ samples with ratios of 30:70 and 45:55 after an air-annealing test at 500 °C for 1000 h. However, despite having parabolic kinetics, the materials grew substantially porous. At 850 °C, bulk TiB_2-$MoSi_2$ with 80:20 ratio experiences pesting during more extended oxidation periods as the surface cracks after 1 h and the protective B_2O_3 evaporates after 4 h. After 16 h, MoO_3 whiskers and the main oxidation product, rutile TiO_2, had formed in the oxide scale. After 64 h, the oxide's weight dropped significantly due to the evaporation of MoO_3. In contrast, the oxides' top layer had become silicon-rich, with only Ti, B, Si, O, and hardly Mo remaining in the whole oxide scale. [76] At 1200 °C, bulk-TiB_2-$MoSi_2$ in a 90:10 ratio built up an amorphous, protective SiO_2 layer after 10 minutes. The 12 h grown scale experienced a decreasing growth rate. It also contained a lesser B and Mo content due to the quick evaporation of their respective oxide products over 1000 °C. [77] A rutile TiO_2 layer covered by a smooth and glassy SiO_2 top layer formed after 24 h. [73] In conclusion, for TiB_2-$MoSi_2$ bulk composites, TiB_2 governs the oxidation behaviour at lower temperatures, while $MoSi_2$ influences the behaviour at higher temperatures significantly.

Additionally, TiB_2-$MoSi_2$ composites exhibit equal RT-hardness compared to monolithic bulk TiB_2, and they display an exceptional combination of hot mechanical properties at 900 °C: TiB_2 with 2.5 wt. % $MoSi_2$ showed a hardness of 10.5 GPa, while the material's flexural strength at RT increased from ~391 GPa to ~503 GPa [27].

$TiSi_2$-based alloying route for $TiB_{2\pm z}$

Another Si-based alloying route followed in this thesis is the TiB_2-$TiSi_2$ composition. For all composition ratios Pugach et al. [23] tested, the TiB_2-$TiSi_2$ system was superior to their pure TiB_2 and $TiSi_2$ bulk counterparts' oxidation kinetics: Low parabolic rates developed in the temperature range of 1000 °C-1200 °C during a duration of 7 h. All composites formed a glassy, protective borosilicate layer. [23] Furthermore, bulk-TiB_2-$TiSi_2$ achieved a comparable hardness to pure TiB_2 at RT with ~25 GPa and superior hot hardness at 900 °C with ~9 GPa for samples with 2.5 wt. %, 5 wt. %, and 10 wt. % $TiSi_2$ content [27]. All $TiSi_2$ alloyed samples analysed by Raju et al. [27] showed crystalline TiB_2 and Ti_5Si_3 phases, whereas the 10 wt. % sample also developed $TiSi_2$ peaks. They observed the Ti_5Si_3 phase formed in the production process during hot pressing [78]. At 1000 °C, all compositions showed TiB_2 and rutile TiO_2 peaks [27]. In the 1990s, TiB_2-$TiSi_2$ bilayer films were first sputter deposited to test them as diffusion barriers: The films turned out amorphous and could not be sufficiently crystallised [79, 80].

Ti_5Si_3-SiB_6-based alloying route for $TiB_{2\pm z}$

The third alloying route followed in this work relied on novel TiB_2-Ti_5Si_3-SiB_6 target compositions. The author found no literature about this precise material system. However, sintering bulk-TiB_2-$TiSi_2$ can lead to a TiB_2-Ti_5Si_3 system and has been tested regarding its properties [27, 78]. Furthermore, arc furnace melted Ti, Si, and B powders create a $Ti_5Si_3B_x$ + TiB_2 (+ Ti_5Si_4) system [81]. Pure Ti_5Si_3 powders exhibited low oxidation kinetics up to 1000 °C for 5 h with TiO_2 as the sole crystalline oxidation product [82].

The sputtering of TiB_2-(Ti_5Si_3-SiB_6) targets aimed to achieve a stoichiometric Ti-Si-$B_{2\pm z}$ system. In thin films, higher Si content was reported to increase the B/Ti ratio, which indicates that Si preferably occupies metal sites in the crystal lattice [28, 29]. DCMS-sputtered TiB_2 thin films are likely overstoichiometric in B [14, 28, 38, 41, 44, 83, 84], whereas HIPIMS-sputtered coatings tend to display a B-deficiency due to higher ionisation potential of B compared to Ti [18, 45]. Further factors of varying influences during sputter deposition of diborides, like the emission angle of elements and various deposition parameters (e.g. pressure, bias voltage), have been extensively discussed in the literature and presented in the following Subchapter [40, 83, 84].

2.2 Sputter deposition

Physical vapour deposition (PVD) designates the physical creation of a vapour phase from a solid, the transfer of the vapour, and its condensation on a substrate creating solid thin films. There, the thin films develop through film nucleation and growth. Importantly, no chemical reactions occur for the transition of the condensed phase to the gas phase, hence the term physical. Different PVD processes produce distinct material properties in the deposited thin films. Therefore, the choice of a deposition technique depends on the application, whereas all PVD processes originate from the following ones: evaporation, sputtering, and ion plating. [85, 86]

In general, PVD techniques need a reduced-pressure vacuum environment, which allows for higher vapour transfer rates and decreases the number of third-party gas molecules contaminating the substrate's surface. The mean-free path describes the vacuum's quality by depicting the average distance between two collisions of atoms or molecules. [85]

For the PVD technique sputtering, one introduces a working gas, usually Ar, into the evacuated PVD chamber to enable a discharge and, eventually, the sputter process. Sputtering occurs by momentum transfer during the bombardment of positively charged ions on the target atoms, which gives the particles the needed energy to leave the target and form vapour. A high negative voltage applied to the target accelerates the positive ions, turning the target into the cathode and igniting a glow discharge. Various events occur by collisions of positively charged ions with the target surface. Some ions are backscattered while others implant themselves into the surface, creating a set of collision cascades in the near-surface region and consequently displacing or sputtering target atoms by momentum transfer (Figure 2.9). Radiation and secondary electrons emit. These effects make different deposition and analytic methods possible. In our case, the sputtered target atoms are of interest: The sputter yield Y measures the efficiency of the sputtering process. One defines Y by the number of atoms or molecules ejected from the target's surface per incident ion: [85–88]

$$Y = \frac{Y_{ejected}}{Y_{incident}} \tag{2.12}$$

The sputter yield Y has a maximum and a minimum threshold for each target element, whereas the latter is the relevant value for sputtering. [88] In the literature, one finds various

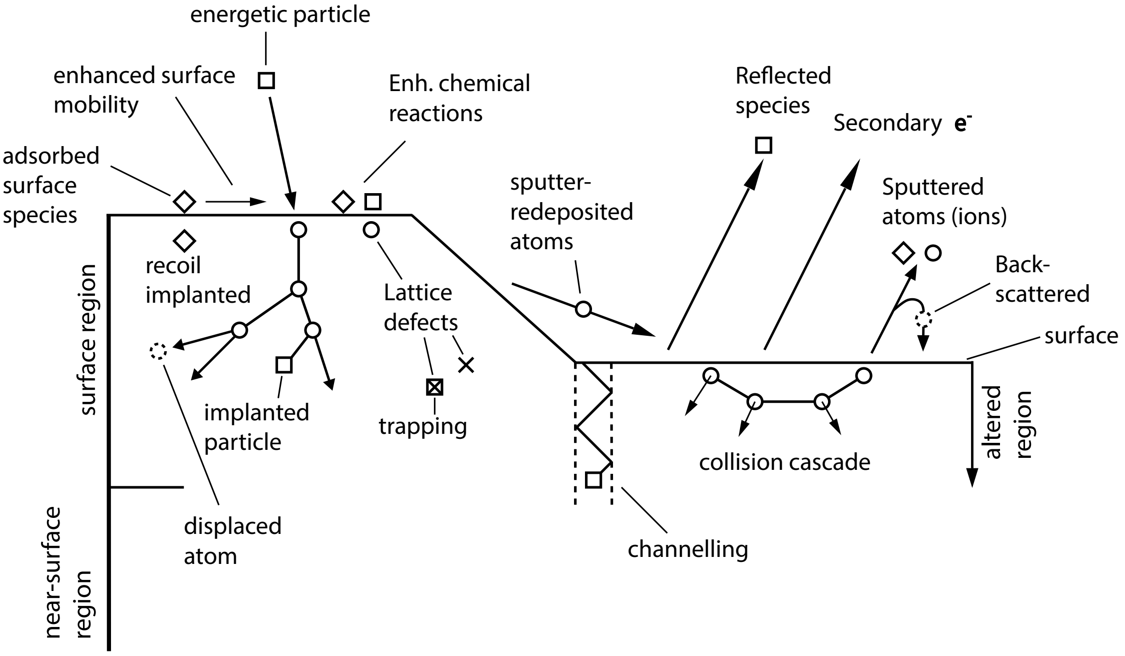

Figure 2.9: Sputter mechanisms at the target's surface area (adapted from [89])

mathematical approaches to determine this threshold [90–93]. The following aspects must be considered: Only a share of displaced atoms moves towards the surface, the number of atomic layers contributing to the reaction must be determined statistically, and the binding energy of the target element, the target density and ion/matrix geometrics must be addressed. Other important factors are the charge applied to the cathode as it controls the ion energy of the plasma and the element-dependent sputter angle. Both control the sputtering rate. [85, 88, 94]

Compared to other PVD techniques sputtering is favoured as it allows a better-sustained target stoichiometry and composition: Sputter yields of different elements differ little from each other, and solid-state diffusion during sputtering is low. Different sputter yields Y are compensated in an A-B system as the element B is sputtered primarily at the instance the sputter surface is A depleted. The resulting short alternating sputtering period adds to a resulting overall steady state, which allows a similar stoichiometry in the deposited thin film. [85, 94]

Nevertheless, a thin film may turn out non-stoichiometric. The deposition distance and the gas pressure are highly influential as collisions happen between sputtered atoms and Ar atoms, which lead to a deflection angle ϕ and a partial thermalisation of the sputtered atom's kinetic energy. If the masses of the colliding atoms are similar, like Ti and Ar, the scattering angle is about 45°, and the thermalisation share maximises. Boron, for example, has a much lower atomic mass than Ar and, therefore, loses less energy through collisions. However, because of its big scattering angle, B will experience more clashes. Thus, a higher gas pressure and a longer deposition distance decrease the amount of deposited B. Additionally, the initial angular distribution of sputtered species strongly influences the growing thin film's stoichiometry. [83, 94, 95] For example, B sputters preferentially normal to the target, while Ti sputters at a shallower angle. Hence, boron's sensitivity to collisions can be exploited by increasing the deposition pressure to avoid a Ti deficiency around the 90° angle. [83]

Direct current magnetron sputtering (DCMS) combines the described sputtering process, in which a charge influences the relative film deposition rate with the impact of an applied magnetic field. Magnets behind the target lead to a magnetic field binding electrons in orbit-like motion near the cathode with its Lorentz force. The plasma concentrates there and increases the probability of ionising a gas atom. Hence, discharge currents and deposition rates increase without increasing the gas pressure, sputtering efficiency improves, and atom-gas collisions reduce. [85, 88]

While sputtering, energised particles arrive at the substrate and charge it. Next, positive Ar-ions are attracted, which attract electrons. Electron and ion fluxes create a stable floating potential between -5 V and -25 V [94]. A negative DC bias voltage can be applied to improve the thin film's properties. This voltage must be low compared to the target voltage. Thus, low-energy ions bombard the growing film making adatoms more mobile to a point at which the adatoms form compact crystalline growth islands. [85, 88] The following parameters are essential for film growth: A high sticking coefficient, the crystallographic orientation of the adatoms, and the adatom mobility. Moderately improving the adatom mobility enhances the growth rate normal to the substrate [88]. At the same time, a high adatom mobility leads to an intergranular exchange of adatoms or re-sputtering depending on the elemental component's individual properties of the thin film alloy. [83, 88] Thus, supposing low adatom mobility, the low energy flux makes diffusion unlikely, which results in straight, clearly facetted columns evolving perpendicular to the substrate. [88] An applied bias voltage can alter properties like hardness, residual stress, density, electrical properties, coverage, film morphology, and adhesion [85].

A higher deposition energy enhances the ionisation of target species. However, during DCMS, the amount of employable power is limited by thermalisation. Nonetheless, one can apply power in a pulsed mode with short duty cycles (t_{on}/T) to achieve high target power densities. These pulse duty cycles are usually less than 10 % of the time cycle. This deposition technique's designation is high-power impulse magnetron sputtering (HIPIMS). It utilises the advantages of magnetron sputtering combined with a high ionisation efficiency of sputtered species. [88, 96] The highly energetic plasma contains a high degree of ionised sputtered atoms increasing the adatom mobility. Consequently, film density and other properties can improve. However, it may also lead to a competitive growth of grains and a decline in property values. [97] Generally, HIPIMS deposition rates are lower than in DC magnetron sputtering. Even though much higher energy peaks are possible, arcing and heat still limit the maximum process power and duration of duty cycles. [88, 96] To achieve convenient HIPIMS deposition parameters, one applies a similar average power measured over a whole period compared to DC magnetron sputtering deposition [98].

Film growth and microstructure

Film growth starts at the moment sputtered atoms arrive at the substrate. Vapour phase atoms form initial nuclei, which either grow or re-evaporate depending on their nuclei's radius (Figure 2.10). [99]

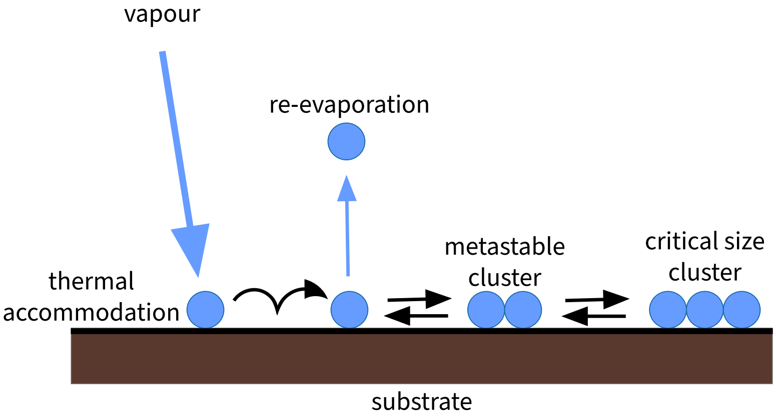

Figure 2.10: Initial nucleation (adapted from [99])

Based on thermodynamics, the tendency to minimise the free energy leads to the formation of atomic clusters, which either grow or dissolve. Supposing a homogeneous, spherical nucleus, the volume-free energy ΔG_V (green in Figure 2.11) is: [85, 99]

$$\Delta G_V = \frac{kT}{\Omega} ln \frac{P_S}{P_V} = -\frac{kT}{\Omega} ln \frac{P_V}{P_S} = -\frac{kT}{\Omega} ln(1+S), \text{ with } S = (P_V - P_S)/P_S \tag{2.13}$$

Where k is the Boltzmann constant, T is the temperature, Ω is the atomic value, P_S is the solid's vapour pressure, and P_V is the equilibrium vapour pressure over the solid. The vapour supersaturation S being >0 is essential as it allows nucleation by reducing the free energy. A nucleus must develop a higher volume of free energy than its surface energy (Figure 2.11, red), as the total free energy (Figure 2.11, blue) is the sum of both. As illustrated in Figure 2.11, the critical radius is at the maximum free energy raised by nucleation: If the nucleus radius r is bigger than r*, it grows; if smaller than r*, it dissolves.

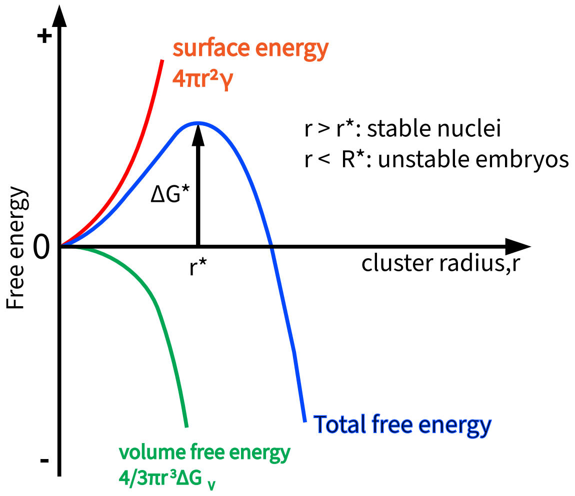

Figure 2.11: Critical nuclei radius (adapted from [99])

Contrary to the simplified model designed to sketch the process, no homogenous nucleation occurs during sputtering because the needed surface energy is less at the substrate. Therefore, the nucleation rate also depends on the substrate temperature, deposition rate, and the substrate's surface condition [85, 99]. Eventually, nucleation depletes, and coalescence takes over. With increasing temperature, island growth happens more distinctively. Also, islands may migrate, merge, and grow in height and width. Merged islands align their crystallographic orientation according to the biggest one.

Three primary film growth modes (Figure 2.12) develop: During three-dimensional island growth, or Volmer-Weber growth, stable nuclei eventually form a continuous film, which occurs when the bond between adatoms is stronger than to the substrate. The two-dimensional, or Frank-van der Merwe growth, covers the opposite, inner-adatom bonds being weaker or equal to adatom-substrate bonds. If the film grows hetero-epitaxially, relaxations mechanisms develop, leading to dislocations in the crystal. The third mode is named after Stranski and Krastanow and depicts a mixture of the previous ones. [99]

Figure 2.12: Thin film growth modes (adapted from [99])

Many factors influence the film formation, including the materials of the film and the substrate, flux J, kinetic energy E, the growth temperature T_S, the flux of contaminants, cleanliness, orientation, and above all, the adatom mobility [99]. Structure zone diagrams (SZD) have been formulated to make the impacts in forming films more comprehensible. Anders [100] drafted the most complete SZD, as seen in Figure 2.13. On the x-axis, logarithmic values for the generalised energy E* describe the displacement and heating effects with a weighted energy flux J from incoming species' kinetic energy: [100]

$$E^* = \frac{\sum_\alpha \frac{E_{kin,\alpha}}{E_C} \frac{m_\alpha}{m_S} J_\alpha}{\sum_\alpha J_\alpha}, \tag{2.14}$$

with $\frac{m_\alpha}{m_S} = 1$, as the mass of incoming energetic particles α and the solid film's particles are identical, with the kinetic energy E$_{kin}$ normalised by the cohesive energy (or heat of sublimation) E$_C$. The generalised temperature T* adds up from the local film growth temperature T and the potential temperature T$_{pot}$. The melting temperature T$_M$ must normalise both to achieve a dimension-wise correct mathematical expression. Hence, the author adapted Anders' equation for T$_{pot}$ by normalising it: [100]

$$T^* = T_h + T_{pot} = \frac{T}{T_M} + \frac{E^*_{pot}}{kN} \frac{1}{T_M} = \frac{T}{T_M} + \frac{1}{kT_M} \frac{\sum_\alpha \frac{E_{pot,\alpha}}{N_\alpha} J_\alpha}{\sum_\alpha J_\alpha}, \tag{2.15}$$

with N being the number of moved atoms and k being the Boltzmann constant. Anders [100] generalised E$^*_{pot}$ like E$^*_{kin}$. T* is found on the y-axis as it depends on E*. Finally, on the z-axis, the film thickness t* is depicted qualitatively to illustrate the changing film thickness under given parameters. Areas with very low T*, high E*, and very low E* values are deemed inaccessible. [100]

Different zones classify the film microstructures, wherein zone 1 covers structures with low deposition rates and negligible adatom mobility. Due to the low temperature, a lack of diffusion results in a fine-grained, porous structure with lattice imperfections. In a higher temperature range, zone T (transition) experiences surface diffusion and competitive grain growth leading to an inhomogeneous structure with V-shaped grains. In zone 2, diffusion occurs within the film bulk, resulting in uniform columnar grains. Grains broaden by further increasing the temperature, eventually leading to pronounced grain growth in the film through recrystallisation (marked with zone 3). [99, 100] The red area in Figure 2.13 marks the ion etching zone, which is used as a pre-deposition step to clean the substrate surface of contamination [100].

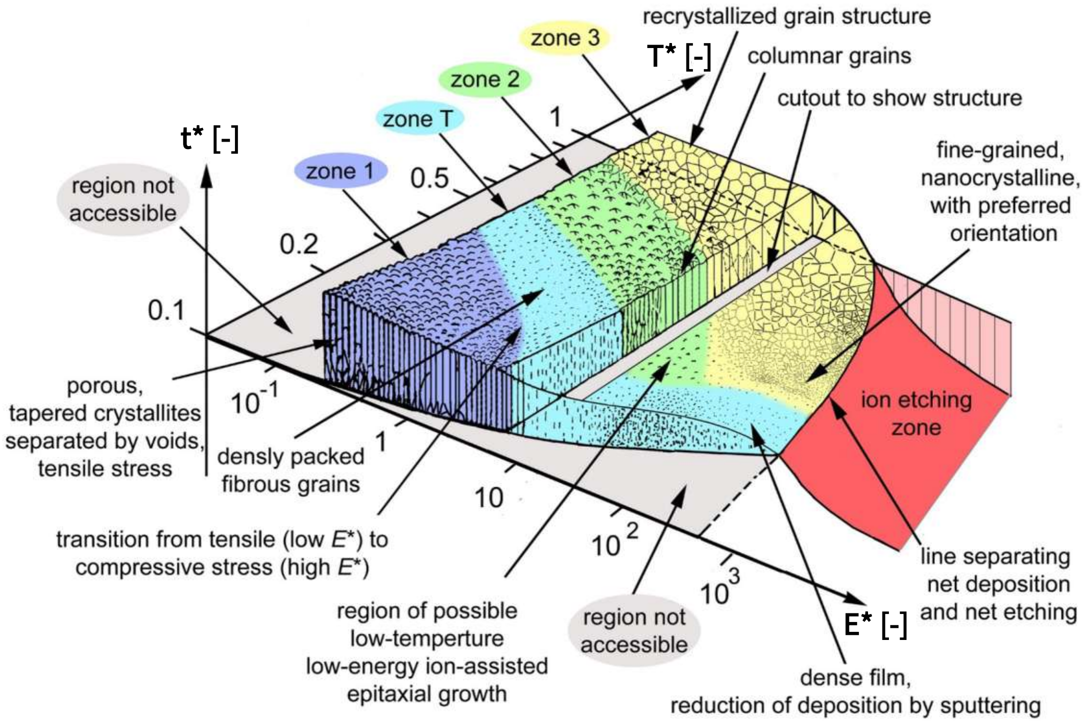

Figure 2.13: Structure zone model by Anders (adapted from [100])

Chapter 3

Methods of analysis

In this Chapter, the author describes the two most extensively used analysis techniques in this work.

3.1 Thermal analysis

3.1.1 Differential scanning calorimetry

In differential scanning calorimetry (DSC), the focus is to measure heat flows and their difference towards the sample and its reference counterpart. Temperature sensors inside the furnace enable the measurement throughout a temperature program. The recorded signal is proportional to the heat flow rate $\Phi(t)$ and must be corrected. A similar method commonly used is the differential thermal analysis (DTA), which measures the temperature difference ΔT for evaluation and interpretation. Regarding DSCs, there are two main types: [101, 102]

The power compensation DSC

Power-compensated DSCs consist of two separate, identical furnaces. One for the sample and one for the reference sample, whereas both furnaces are heated equally at the start. During the test, a temperature asymmetry can and will occur from sample reactions. When this happens, power is introduced into or removed from the sample furnace to compensate for the temperature difference ΔT. The needed compensation power produces the primary measurement signal, hence, the name. [101–103]

The heat flux DSC

In heat flow DSCs, the sample and the reference crucible are located in a single furnace, and the primary measurement signal is the temperature difference ΔT [101]. There must be a temperature difference between the sample, reference, and furnace for heat flow. Thus, the heat flow signal $\Phi(T)$ results from the difference of the heat flows from the sample sensor and the reference sample sensor divided by the thermal resistance $R_{th}(T)$ of the sensors: [104]

$$\Phi = \frac{T_s - T_r}{R_{th}(T)} \tag{3.1}$$

The original thermoelectric voltage V of the sensor thermocouples determines the sensitivity S: [104]

$$S(T) = \frac{V}{T_s - T_r} \rightarrow \Phi = \frac{V}{R_t h(T) S(T)} = \frac{V}{E(T)}, \tag{3.2}$$

wherein E is the temperature-dependent calorimetric sensitivity [104]. Alternatively, a standard reference sample, with known enthalpy ΔH and mass m, is tested over the time integral of the temperature difference: [103]

$$S(T) = \frac{m_{standard} \Delta H_{standard}}{\int_{t_1}^{t_2} \Delta T(t) dt} \tag{3.3}$$

The constant time lag, produced by the thermal resistance R_{th}, adds to the calculated temperature increase ΔT. Moreover, the sensitivity S includes the slight temperature difference between the sample and the sensor. The DSC's software includes explicitly set sensitivities S and E to calculate the sample temperature T_s: [104]

$$\Phi = \frac{T_s - T_r}{R_{th}(T)} \rightarrow T_s = T_r + \Phi T_{th} \frac{S}{S} = T_r + \Phi \frac{E}{S} \tag{3.4}$$

The onset temperature T_{onset} must be known to calibrate a heat flux DSC. It marks the first detectable deviation from the baseline heating curve [103].

3.1.2 Thermogravimetric analyser

A thermogravimetric analyser (TGA) records a mass signal to identify mass gains and losses during thermal analysis. The measured signal is the material mass as a function of temperature or time, changing due to oxidation, decomposition, dehydration, desorption, or evaporation. [101–103] TGA designs differ depending on the balance-sample arrangement towards each other. Also, the test atmosphere in the furnace must be considered and corrected accordingly because the fluid mechanical buoyancy force varies with the gas mix present. [104]

3.1.3 Simultaneous thermal analyser

A simultaneous thermal analyser (STA or single differential thermal analyser (SDTA) can simultaneously record a DSC and a TGA. Before an STA measurement, one must make sure the furnace, crucible, sensors, and sample are suitable for the planned test program and not contaminated to achieve a precise and repeatable measurement [101, 104–106]. To clean, one introduces heat into the chamber [104] or evacuates the chamber to form a vacuum [85, 105]. Afterwards, a protective, inert gas purges the furnace. This gas might be helium (up to 1300 °C) or argon for high-temperature tests. For the creation of varying measurement conditions, gases like nitrogen and oxygen are also needed. Finally, a baseline (correction) measurement with an empty sample is required for reproducibility. [104, 105]

At the start of the measurement, the sample is homogenised at an elevated temperature (Figure 3.1) for a certain period. This period is an isothermal segment and presents a repeatable starting point. Next, a dynamic segment is added, where the temperature rises by a specific heating rate. [104] The user can conduct various measurements by combining dynamic and isothermal segments. Possible categories of temperature programs are dynamic, iso-stepwise, and areas methods (last one not used in this work, all in Figure 3.2), wherein each heating phase can have its separate gas atmosphere. [102, 105] The sample's heat capacity leads to a temperature difference between the sample (T_s) and reference (T_r) crucible. At the sample's melting point, for example, its temperature remains constant while T_r steadily increases as melting is an endothermic reaction that consumes enthalpy. After completing the reaction, the initial temperature difference T_r-T_s is re-established by a rapid temperature rise of the sample. Another isothermal segment leads to a temperature equilibrium in the whole furnace. The following dynamic segment decreases the temperature to close the temperature cycle. Beneath the crystallisation temperature, the sample re-crystallises, leading to an increase in the sample temperature. At the same time, the temperature decrease of T_r stays steady. After the exothermic reaction completes, T_s re-aligns again. [104]

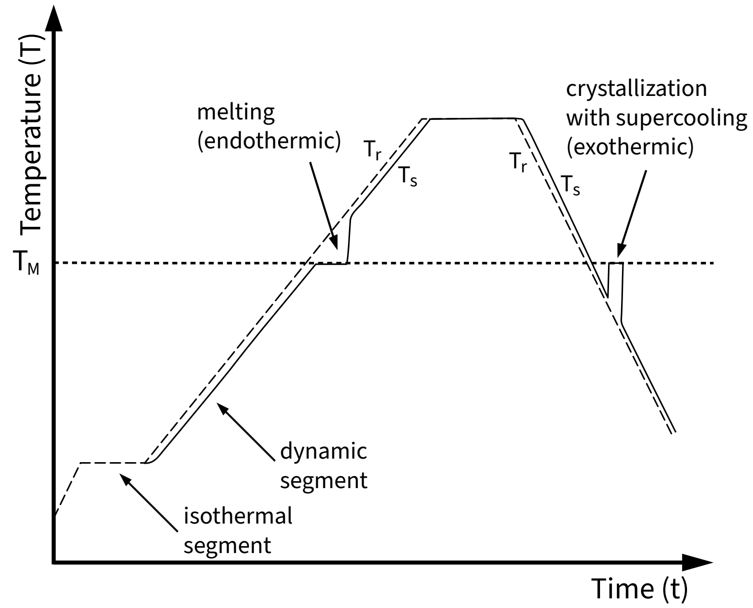

Figure 3.1: Dynamic temperature program (adapted from [104])

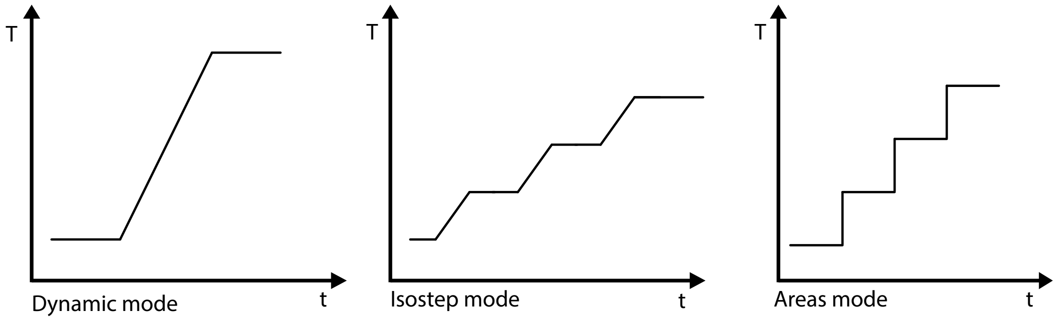

Figure 3.2: Temperature program modes (adapted from [102])

3.2 X-ray diffraction analysis

Structural analysis with X-ray diffraction (XRD) is non-destructive and enables characterising material properties regarding the chemical composition and crystalline structure. Collisions with atoms scatter a share of the incoming X-rays from the sample into all directions. In the case of positive interference called diffraction, coherently scattered (elastic scatters with inner-shell electrons) X-rays bundle at a particular angle from the sample plane, producing a high intensity, hence, a strong signal. [107, 108] For this case to happen and assuming X-rays from the source are in phase, sample atoms must be aligned periodically in a crystalline fashion. The additional distance X-rays, which have been deflected in a lower plane of the sample, must equal a factor n (n $\in \mathbb{N}$) of the wavelength λ to create the diffraction (Figure 3.3).

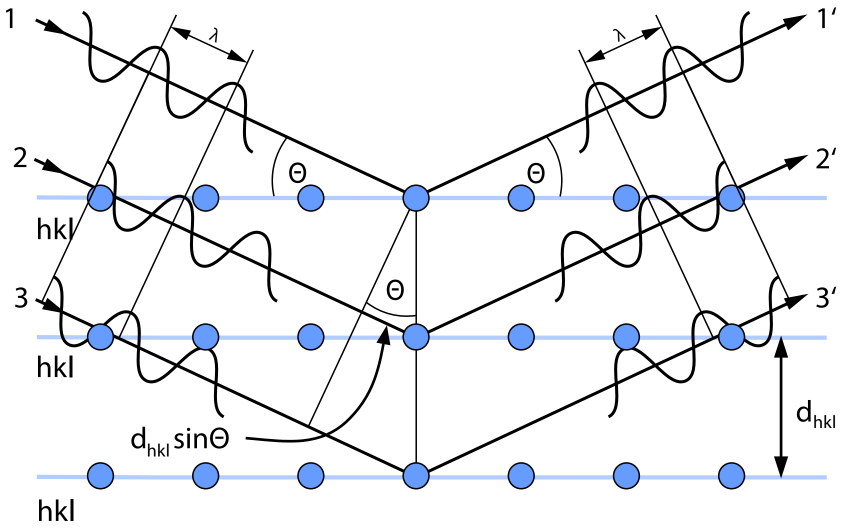

Figure 3.3: Bragg's law

The diffraction angle depends on the crystal structure of the sample. [108] This effect reflects in Bragg's law: [107–109]

$$2d_{hkl} \cdot \sin(\Theta) = n\lambda, \tag{3.5}$$

d$_{hkl}$ is the distance between two atomic layers, and Θ is the angle between the X-ray source and the sample's nuclear surface. On the other end of the equation, n is the order of the interference (n = 1,2, ...), and λ is the wavelength of the X-rays. [107]

The Miller indices *hkl* characterise the orientation and the distance d$_{hkl}$. Hence, one can derive with a given d-value the lattice parameters using the quadratic formulas as the one for the cubic (3.6) and the tetragonal (3.7) crystal structure: [107]

$$\frac{1}{d^2} = \frac{h^2 + k^2 + l^2}{a^2} \tag{3.6}$$

$$\frac{1}{d^2} = \frac{h^2 + k^2}{a^2} + l^2 a^2 \tag{3.7}$$

Miller indices *hkl* are the reciprocals of the fractional coordinates of the axial intercepts of a cartesian coordinate system. As an example, for a (102) plane, one takes one step in the 'a' direction and a half in the 'c' direction to find the intercepts (Figure 3.4): [107, 108]

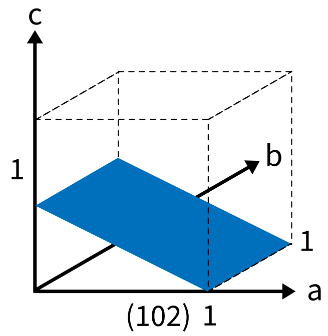

Figure 3.4: Crystal plane determined by Miller indices

Crystal structures are grouped into 14 Bravais lattices (fixed by the parameters a, b, c, and α, β, γ), 32 crystal classes (symmetry groups), and 230 unique space groups that combine crystal classes and Bravais lattices. [107] The regular arrangement of the crystal structure in the sample leads to strengthened diffractions at specified angles. The resulting data is put into a diffractogram, illustrating the intensity in arbitrary units over the diffraction angle 2Θ (°). If a peak appears narrow, the crystallinity is high, whereas the broader a peak, the higher the amorphous share or the share of third-party elements in the crystal structure. The intensity of thin film coatings in the resulting data is generally limited because the number of atomic planes in the sample is finite. [107, 108]

2Θ-angles of expected intensity peaks can shift due to stresses within the film or the sample's placement in the false height. Furthermore, factors like absorption and symmetry, orientation, and position of the crystal structure determine the intensity of a peak. There is also coherent and incoherent scatter and fluorescence emitted from the sample, leading to background noise. Impurities are the main reason for the appearance of artefacts in the data. [107, 108]

One can also conduct XRD analyses in non-ambient environments like under temperature programs, vacuum, or gas atmospheres. Of particular interest for UHTC thin films are in situ XRD measurements: The analysis takes place during a temperature program in a vacuum or gas atmosphere. The XRD analyser needs special equipment like vacuum chambers, heating, temperature sensors, and height adjustment options for such tests. The latter must be calibrated at the beginning of each measurement and actively software-controlled during the experiment. [107]

3.2.1 Bragg-Brentano and grazing incidence

There are two main reflection modes for XRD analysis: The Bragg-Brentano configuration (Figure 3.5a) is either in Θ:Θ (the preferred one) or Θ:2Θ setting and preferably in a vertical setup to prevent spilling of powder or liquid/melt samples. The sample platform moves independently of the goniometer, which rotates the X-ray source and the detector at equal scanning speed at a constant radius R around the sample. The main drawback when using the standard Bragg-Brentano method for thin film samples is that the substrate peaks are also visible in the resulting X-ray diffractogram. If the substrate's peaks are known, they can be marked and excluded from further investigation. [107, 108]

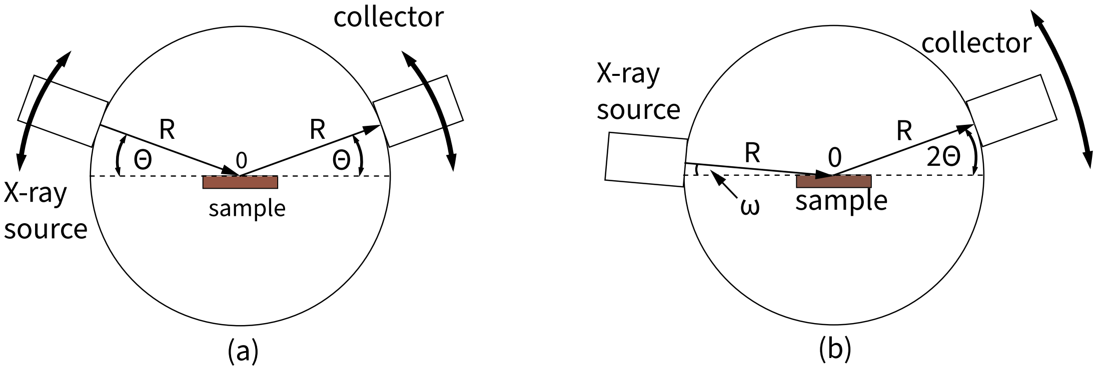

Figure 3.5: Vertical XRD setup with the (a) Bragg-Brentano method and (b) grazing incidence method

The second method, grazing incidence, can register higher intensities of the thin film as it is more concentrated towards the surface area than the standard Bragg-Brentano method. [107] In a grazing incident setup (Figure 3.5b), a fixed low glancing angle ω avoids the measurement of the substrate while including the whole coating. The detector moves with an angle of 2Θ, capturing diffracted X-ray beams from the surface area. Also, when deploying grazing incidence, the XRD is converted into a non-focusing XRD resulting in a significant intensity loss which leads to extended measurement durations. [110, 111]

Chapter 4

Experimental Details

4.1 Coating depositions

For this work, an in-house developed physical vapour deposition (PVD) system named 'FRIDA' [112, 113] served for non-reactive direct current and high-power impulse magnetron sputtering. This PVD system can be equipped with a single 3-inch target. Table 4.1 lists the alloys of the TiB_2-based targets, which were sputtered in this work and have been provided by Plansee Composite Materials GmbH [114].

Table 4.1: Compositions of targets sputtered in this work

Target composition	**Composition ratio [mol.%]**
$TiB_2/TiSi_2$	90/10
$TiB_2/TiSi_2$	80/20
$TiB_2/Ti_5Si_3/SiB_6$	77.12/8.58/14.30
$TiB_2/Ti_5Si_3/SiB_6$	58.89/15.44/25.67
$TiB_2/MoSi_2$	85/15
$TiB_2/MoSi_2$	80/20

For the depositions, we used polycrystalline Al_2O_3 substrates (20×7×0.38 mm), single crystalline Al_2O_3 (sapphire in $10\bar{1}1$ orientation, 10×10×0.53 mm), single-crystalline Si (100-oriented, 20×7×0.38 mm), and mild steel foil with a thickness of 0.025 mm [115]. In preparation prior to the depositions, these substrates were cleaned by submerging them into a hypersonic bath using acetone and ethanol consecutively for 5 minutes each. Afterwards, the substrates were further cleaned in the PVD chamber for 10 min by Ar^+ etching at a substrate bias potential of -800 V and 180 standard cubic centimetres per minute (sccm) of Ar gas, resulting in a pressure of ∼49 µbar. Furthermore, the targets were sputter cleaned under a closed shutter lid to eliminate any remaining surface contamination without polluting the substrates.

Table 4.2 summarises all the deposition parameters applied during thin film depositions. All targets were sputtered, applying the non-marked and general parameters. Moreover, two series of coatings were deposited from a selected target ($TiB_2/MoSi_2$ [80/20]) using two different schemes of varied substrate bias voltage (bias series) and a high-power impulse magnetron sputtering (HIPIMS series). Additional to the parameters indicated in Table 4.2, for the bias series, we applied -80 V, -100 V, -120 V, and -150 V substrate bias voltage. The HIPIMS series was deposited with a frequency of 1 kHz and varied pulse duty cycles (d.c.) of 2.5 %, 5 %, and 10 %.

Table 4.2: Applied deposition parameters

Deposition parameter	**Value [unit]**
Applied target current^{1,2}	0.5 [A]
Ar gas flow	23 [sccm]
Deposition duration^{1,2}	180^{1,2}, 240^{3} [min]
Deposition pressure	4 [µbar]
Sample holder rotation speed	0.25 [Hz]
Sample temperature	550 [°C]
Substrate bias voltage^{1,3}	-40 [V]
Target-to-substrate distance	90 [mm]

[1] general parameter
[2] bias coatings series
[3] HIPIMS coatings series

4.2 Chemical analysis

We used as-deposited Ti(-Mo)-Si-$B_{2\pm z}$ thin films grown on sapphire substrates for the chemical analysis. The ion beam analysis techniques of elastic recoil detection analysis (ERDA) and Rutherford backscattering (RBS) were employed to determine the chemical composition of the as-deposited coatings. Furthermore, inductively coupled plasma-optical emission spectroscopy (ICP-OES) was used as a complementary chemical analysis method for all films.

4.3 Microstructure

To investigate the microstructure of the TiB_2-based thin films, we used a secondary electron microscope (SEM, Zeiss Sigma 500 VP [116]). The deployed acceleration voltage was 3 kV, and the working distance was ~10 mm for all cross-sections. We chose films on Si-substrates for cross-sectional investigations of as-deposited coatings, whereas Al_2O_3 substrates were used for the oxidised films' cross-sections. During the SEM investigations, we had to apply liquid silver to the oxidised films to ensure sufficient conductivity of the fractured surfaces.

The obtained film thickness of the DCMS as-deposited coatings is in the range of ~1.96 µm for the $Ti_{0.26}Si_{0.15}B_{0.59}$ film and ~3.46 µm for the $Ti_{0.23}Mo_{0.07}Si_{0.17}B_{0.53}$ film. Therefore, the deposition rates varied between ~10.89 nm/min and ~19.22 nm/min. For the bias series, the film thickness declined from ~3.46 µm for the -40 V sample to ~2.65 µm for the -150 V sample reflecting the lowest deposition rate of ~14.7 nm/min. As the deposition duration of the HIPIMS series was longer than that of all other depositions (see Table 4.2, deposition duration [3]), the deposition rate ranging from ~18.24 nm/min for the 10 % pulse duty cycle (d.c.) deposited film to ~14.45 nm/min for the 2.5 % d.c. deposited film is the parameter to for comparisons.

We used a transmission electron microscope (TEM, FEI TECNAI F20 [117]) to take brightfield and darkfield cross-sectional images of $Ti_{0.23}Mo_{0.07}Si_{0.17}B_{0.53}$ films 1 h isothermally oxidised at 1000 °C and 1200 °C in ambient air. The electron diffraction and chemical analyses using electron energy loss spectroscopy (EELS) mapping were conducted in the same system. EELS precision in identifying lower mass elements leads to the accurate measurement for the oxidised Ti-Mo-Si-B system.

$Ti_{0.23}Mo_{0.07}Si_{0.17}B_{0.53}$ coatings long-time oxidised up to 60 h at 1200 °C were investigated with a ThermoFisher Scios II [118], a focused ion beam-secondary electron microscope (FIB-SEM dual beam). To prepare the cross sections, rough milling with a current of 7 – 15 nA and 1 nA for fine milling at an acceleration voltage of 30 kV was applied. We conducted an energy dispersive X-ray spectroscopy (EDX) investigation in the same system.

4.4 Crystal structure investigation

We conducted XRD analyses in the Bragg-Brentano configuration using an X'Pert MPDII equipped with a Cu-Kα radiation source [119] to determine the crystal structure and phase transformations of as-deposited and isothermally oxidised samples. Due to the B-B measurement method, substrate peaks of polycrystalline Al_2O_3 are visible in all diffractograms except the ones of powdered samples.

In-situ XRD measurements were done on powdered sample material of the $Ti_{0.23}Mo_{0.07}Si_{0.17}B_{0.53}$ film. The coated iron foil was dissolved in hydrochloric acid to obtain the powder material. The coating flakes were subsequently cleaned using ethanol and ground to powder. The powder sample was in-situ vacuum annealed in an XRD (X'Pert MPDIII [119]) up to 1200 °C to investigate phase transformations independent of oxygen, substrate, and tensile stresses. After evacuating the chamber and establishing a vacuum, we calibrated the height of the sample in the machine. The first measurement took place at 25 °C and then from 100 °C to 500 °C in 100 °C steps. From 500 °C to 1200 °C, the step size was reduced to 50 °C. After cooling down, the powder was remeasured at 50 °C. The data was unreliable for measurements above 1100 °C as residual oxygen from the furnace wall reacted with the powdered coating for the in-situ vacuum annealing test. In the same machine and temperature program, an in-situ ambient air oxidation XRD measurement in grazing incidence configuration was conducted for the $Ti_{0.23}Mo_{0.07}Si_{0.17}B_{0.53}$ film deposited on polycrystalline Al_2O_3. The fixed ω-angle was 3°.

4.5 Mechanical property measurements

We used an ultra-micro indentation system (UMIS) with a mounted diamond Berkovich tip to determine the films' hardness and elastic modulus in a line measurement of 30 indents and a force range from 3 to 45 mN. All tested coatings have grown on sapphire substrates and were measured in the as-deposited state.

For calculating the E-modulus, the author chose the Poisson's ratio ν=0.15 for pure TiB_2 [120] as it is the deposited films' main phase. The author defined data blips as ones differing with a factor of >1.3 from the arithmetic mean value: These blips were removed from the collected data before recalculating the arithmetic mean and the standard deviation.

4.6 Thermal analysis

We oxidised the Ti(-Mo)-Si-$B_{2\pm z}$ coated polycrystalline Al_2O_3 substrates using a combined DSC/TGA system Netzsch STA 449 F1 [106] in a dynamic temperature program. During all tests on this system, protective He gas was constantly flowing at 20 ml/min, and during the oxidation segments, an O_2/N_2-gas mixture (80/20 ratio) at a flowing rate of 50 ml/min was added.

The first test was a dynamic oxidation program up to 1400 °C at a 10 K/min heating rate. Afterwards, the author conducted 1 h isothermal oxidation tests at temperatures ranging from 700 °C to 1000 °C for ternary Ti-Si-B films and from 800 °C to 1200 °C for Ti-Mo-Si-B films, depending on the relevant data derived from the dynamic oxidation tests.

Furthermore, selected Ti(-Mo)-Si-$B_{2\pm z}$ films deposited on polycrystalline Al_2O_3 were oxidised in an ambient using a conventional box furnace for 1 h at 1000 °C and 1200 °C. At 1200 °C, coatings grown on sapphire substrates were long-time oxidised for 3 h, 10 h, 30 h, 60 h, and 100 h.

Chapter 5

Results & Discussions

5.1 As-deposited coatings

5.1.1 Chemical analysis

Table 5.1 contains the chemical compositions for the films sputtered from targets listed in Table 4.1. The ternary Ti-Si-B coatings are written into the first four rows and the quaternary Ti-Mo-Si-B films into the last two rows. The stoichiometry of the films was calculated by B/Me, wherein Me is Ti + Mo.

In the first row, the $Ti_{0.25}Si_{0.08}B_{0.67}$ film displays a distinct B excess with B/Me >2 (most right column in Table 5.1) and a small Si content. The $Ti_{0.26}Si_{0.15}B_{0.59}$ film (row 2 in Table 5.1 and Table A.1 in the appendix) exhibits a B/Me overstoichiometry with an increased Si-content. Coatings sputtered from the targets of the second ternary composition (measured by ICP-MS, rows 5 and 6 of Table 5.1) show consistently overstoichiometric films with B/Me ∼3: The two films exhibit similar compositions wherein $Ti_{22}Si_{0.13}B_{0.65}$ has a slightly higher Si and Ti content and a little lower B content than the $Ti_{21}Si_{0.13}B_{0.66}$ film. The films' Si content is between the $Ti_{0.25}Si_{0.08}B_{0.67}$ and the $Ti_{0.26}Si_{0.15}B_{0.59}$ films' measured values.

The quaternary $Ti_{0.24}Mo_{0.05}Si_{0.12}B_{0.59}$ coating (5th row in Table 5.1 and Table A.1) shows almost perfect stoichiometry and an Si content of about 11.6 at. %. The $Ti_{0.23}Mo_{0.07}Si_{0.17}B_{0.53}$ coating (last row of Table 5.1 and Table A.1) depicts B understoichiometry with B/Me ∼1.78 and an increased Si amount compared to the $Ti_{0.24}Mo_{0.05}Si_{0.12}B_{0.59}$ coating.

Table 5.2 displays the chemical compositions of the series deposited with varying substrate bias voltage. With increasing the bias voltage, the Ti-, Mo-, and B-contents increase continuously and moderately while the amount of Si in the coatings declines.

The -100 V coating composition estimated from the ERDA-RBS data (3rd row in Table 5.2) marks an outlier not confirmed by the ICP-OES analysis (3rd row in Table A.2 in the

Table 5.1: ERDA-RBS chemical analysis of the DCMS as-deposited films with calculated B/Me stoichiometry

Thin film	**Target composition**	**Element concentration from ERDA - RBS**					**B/Me ratio**
	[mol.%]	**Ti [at.%]**	**Mo [at.%]**	**Si [at.%]**	**B [at.%]**	**O [at.%]**	**[-]**
Ti$_{0.25}$Si$_{0.08}$B$_{0.67}$	TiB$_2$/TiSi$_2$ [90/10]	23.9	-	7.6	65.5	2.6	2.74
Ti$_{0.26}$Si$_{0.15}$B$_{0.59}$	TiB$_2$/TiSi$_2$ [80/20]	25.7	-	14.2	58.2	1.67	2.27
Ti$_{21}$Si$_{0.13}$B$_{0.66}$ *	TiB$_2$/Ti$_5$Si$_3$/SiB$_6$ [77.12/8.58/14.30]	21.58	-	12.84	65.58	-	3.04
Ti$_{22}$Si$_{0.13}$B$_{0.65}$ *	TiB$_2$/Ti$_5$Si$_3$/SiB$_6$ [58.89/15.44/25.67]	21.63	-	13.30	65.07	-	3.01
Ti$_{0.24}$Mo$_{0.05}$Si$_{0.12}$B$_{0.59}$	TiB$_2$/MoSi$_2$ [85/15]	23.3	5.2	11.6	57.4	2.2	2.01
Ti$_{0.23}$Mo$_{0.07}$Si$_{0.17}$B$_{0.53}$	TiB$_2$/MoSi$_2$ [80/20]	22.7	6.6	16.2	52.2	2.1	1.78

* Measured by ICP-MS

appendix), and the coating deposited with an applied bias voltage of -150 V exhibits a considerably declined Si content. All coatings of the bias voltage series above a negative bias voltage of -80 V are consistently understoichiometric with B/Me ~1.6. Therefore, the Si content is the only distinct change in the films' chemical compositions. The observed decline in Si at higher bias voltage may be owing to preferential resputtering of Si due to the species' low atomic mass and surface binding energy.

Table 5.2: ERDA-RBS analysis of Ti-Mo-Si-B films sputtered from the TiB$_2$/MoSi$_2$ [80/20] target in a bias voltage series with calculated B/Me stoichiometry

Thin film	**Bias voltage**	**Element concentration from ERDA - RBS**					**B/Me ratio**
	[V]	**Ti [at.%]**	**Mo [at.%]**	**Si [at.%]**	**B [at.%]**	**O [at.%]**	**[-]**
Ti$_{0.23}$Mo$_{0.07}$Si$_{0.17}$B$_{0.53}$	-40	22.7	6.6	16.2	52.2	2.1	1.78
Ti$_{0.25}$Mo$_{0.08}$Si$_{0.14}$B$_{0.53}$	-80	24.5	7.3	14.1	52.2	0.9	1.64
Ti$_{0.25}$Mo$_{0.07}$Si$_{0.17}$B$_{0.51}$	-100	24.3	7.2	16.9	49.3	2.1	1.57
Ti$_{0.27}$Mo$_{0.07}$Si$_{0.12}$B$_{0.54}$	-120	26.3	7.3	11.4	54.0	0.9	1.61
Ti$_{0.28}$Mo$_{0.08}$Si$_{0.08}$B$_{0.56}$	-150	28.0	7.8	8.0	55.0	0.9	1.54

Table 5.3 contains the chemical composition of the HIPIMS deposited series compared to the DCMS-deposited Ti-Mo-Si-B film. The film deposited with the 10 % pulse duty cycle (row 2 of Table 5.3) achieved a very similar composition to the DCMS deposited film (row 1 of Table 5.3) with a decreased Si content and an increased Ti content. The HIPIMS series deposited coatings (rows 2 to 4) display only one considerable composition difference with the 10 % d.c. deposited coating showing lower Ti-content (of ~3 at. %, row 2 of Table 5.3) compared to the films deposited with a 2.5 % d.c. and a 5 % d.c.. Other changes, like the slight decrease in Mo- and Si-content, cannot be commented on as only one coating was measured for every pulse duty cycle.

Table 5.3: ICP-OES chemical composition analysis of the HIPIMS-deposited series sputtered from the $TiB_2/MoSi_2$ [80/20] target in the as-deposited state

Thin film	**Pulse duty cycle**	**Element concentration from ICP - OES**					**B/Me ratio**
Frequency 1kHz	[V]	**Ti** [**at.%**]	**Mo** [**at.%**]	**Si** [**at.%**]	**B** [**at.%**]	**O** [**at.%**]	[-]
$Ti_{0.23}Mo_{0.07}Si_{0.17}B_{0.53}$ *	DCMS	22.7	6.6	16.2	52.2	2.1	1.78
$Ti_{0.26}Mo_{0.07}Si_{0.14}B_{0.53}$	10	25.87	6.58	13.95	53.60	-	1.65
$Ti_{0.28}Mo_{0.07}Si_{0.14}B_{0.51}$	5	28.05	6.44	13.66	51.86	-	1.50
$Ti_{0.28}Mo_{0.06}Si_{0.14}B_{0.52}$	2.5	28.19	6.00	13.65	52.16	-	1.53

* Measured by ERDA-RBS

5.1.2 Microstructure

In the following figures, the dashed lines indicate interfaces between the substrate, coating, and surface. The films' deposition rates, thicknesses, and the substrates used are discussed in the experimental details (Subchapter 4.3).

Figure 5.1 shows cross-sections of all coatings in the as-deposited state, wherein the grainy interface is the fracture interface originating from breaking the samples. In the cross-sections of the films $Ti_{0.25}Si_{0.08}B_{0.67}$ in Figure 5.1a, $Ti_{0.26}Si_{0.15}B_{0.59}$ in Figure 5.1b, $Ti_{21}Si_{0.13}B_{0.66}$ in Figure 5.1c, $Ti_{0.24}Mo_{0.05}Si_{0.12}B_{0.59}$ in Figure 5.1e, and $Ti_{0.23}Mo_{0.07}Si_{0.17}B_{0.53}$ in Figure 5.1f at least some segments show the intrinsic interface. These intrinsic sections exhibit a fine columnar microstructure, while the $Ti_{22}Si_{0.13}B_{0.65}$ film in Figure 5.1d appears featureless, which can be attributed to the Si alloying content in the TiB_2-based coatings. In support of this claim, the reader can see the least Si-alloyed film ($Ti_{0.25}Si_{0.08}B_{0.67}$ film in Figure 5.1a) displaying the broadest, most pronounced columns of Figure 5.1.

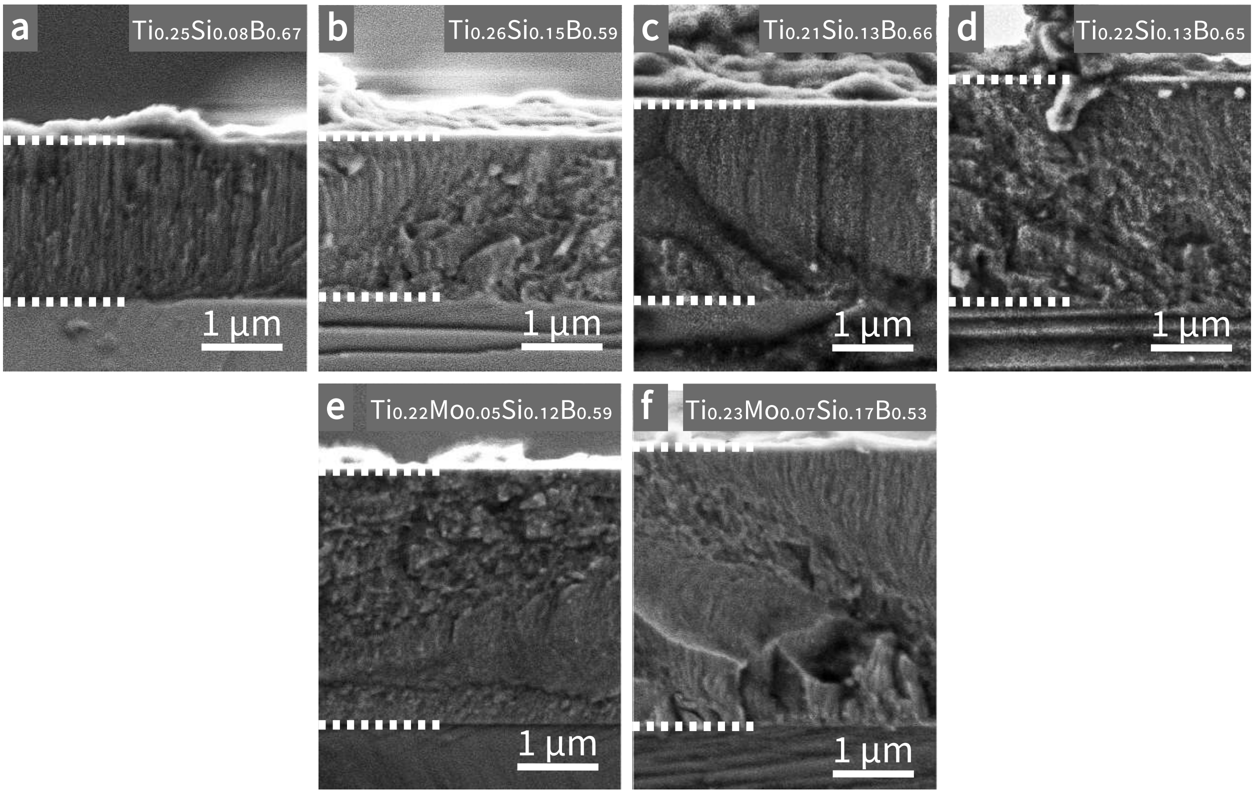

Figure 5.1: SEM cross-sectional images of DCMS thin films on Si substrates in the as-deposited state: (a) $Ti_{0.25}Si_{0.08}B_{0.67}$, (b) $Ti_{0.26}Si_{0.15}B_{0.59}$, (c) $Ti_{21}Si_{0.13}B_{0.66}$, (d) $Ti_{22}Si_{0.13}B_{0.65}$, (e) $Ti_{0.24}Mo_{0.05}Si_{0.12}B_{0.59}$ and (f) $Ti_{0.23}Mo_{0.07}Si_{0.17}B_{0.53}$;

Figure 5.2 shows the cross-sections of as-deposited films from the bias voltage series. The columnar microstructure got finer with increasing negative bias voltage (from Figure 5.2a to e), and the film thickness declined continuously. The -120 V coating's (Figure 5.2d) columnar microstructure is harder to notice: The fine columns are visible in the near-surface and near-substrate regions. The observed decrease in film thickness may stem from increased film density and resputtering effects at higher bias voltages.

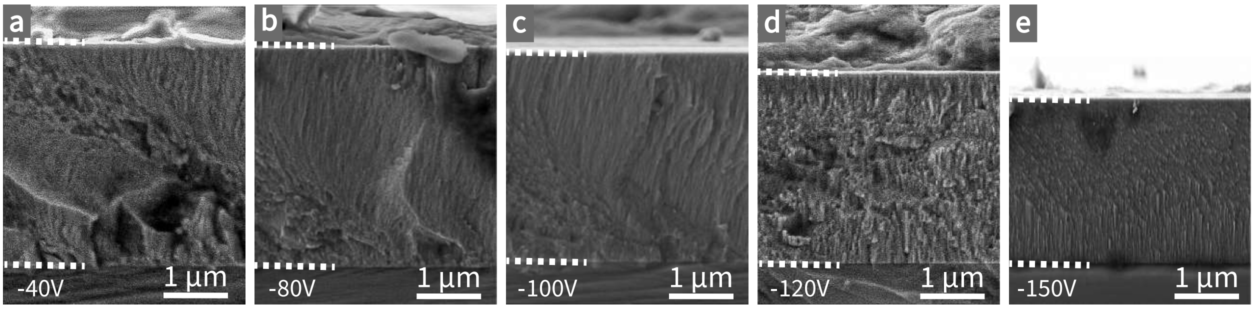

Figure 5.2: SEM cross-sectional images of bias substrate voltage-series sputtered from the $TiB_2/MoSi_2$ [80/20] target on Si substrates in the as-deposited state: (a) - 40 V, (b) - 80 V, (c) - 100 V, (d) - 120 V, (e) - 150 V

Figure 5.3 shows the SEM cross-sectional images of the HIPIMS deposited films (Figure 5.3b to d) compared to the DCMS deposited $Ti_{0.23}Mo_{0.07}Si_{0.17}B_{0.53}$ film (Figure 5.3a). The film thickness is not comparable as the deposition time differs (see the depositions parameters in Table 4.2). The intrinsic features within the cross-section of the coating deposited with the 10 % d.c. (Figure 5.3b) displays visible fine columnar microstructure, and the coating deposited with a 5 % d.c. (Figure 5.3c) looks featureless. A super-fine columnar microstructure can be seen in the 2.5 % d.c. deposited film in Figure 5.3d due to the intrinsic and fracture interface mixture.

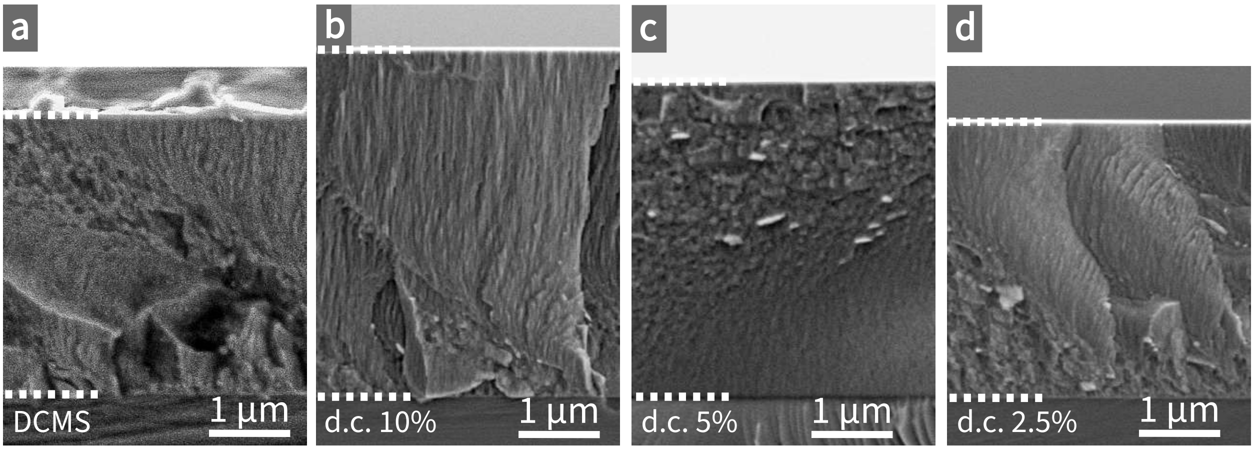

Figure 5.3: SEM cross-sectional images of HIPIMS-deposited coatings sputtered from the $TiB_2/MoSi_2$ [80/20] target on Si substrates in the as-deposited state: (a) DCMS, (b) duty cycle 10 %, (c) duty cycle 5 %, (d) duty cycle 2.5 %

5.1.3 Crystal structure

Figure 5.4 depicts the XRD scans of the thin films sputtered from the targets listed in Table 4.1. All Ti(-Mo)-Si-$B_{2\pm z}$ films display the hexagonal TiB_2 phase (space group number 191, blue lines) with a dominant (001) peak at ~27.6°. TiB_2 is the only detected phase for the ternary Ti-Si-B coatings (blue curves in 5.4), while the diffractograms Ti-Mo-Si-B films (green curves in 5.4) exhibit broadened peaks at ~28° and ~44.5°. Additionally, their ~34° peaks show higher intensities. The quaternary Ti-Mo-Si-B's peak positions indicate a single-phase solid solution with the AlB_2-structured type. The hexagonal MoB_2 phase (green lines) fits nicely into the X-ray diffractograms, suggesting the solid solution is being named a $Ti(Mo)B_2$ phase.

The distribution of Si within the as-deposited coatings is unclear at this point. No indication for a crystalline phase suggests its presence either at grain boundaries or in a solid solution. The shift of all peaks, including the substrate peaks of the polycrystalline Al_2O_3 (ochre lines), towards high 2Θ values can most probably be attributed to an inaccurate sample height during the measurements.

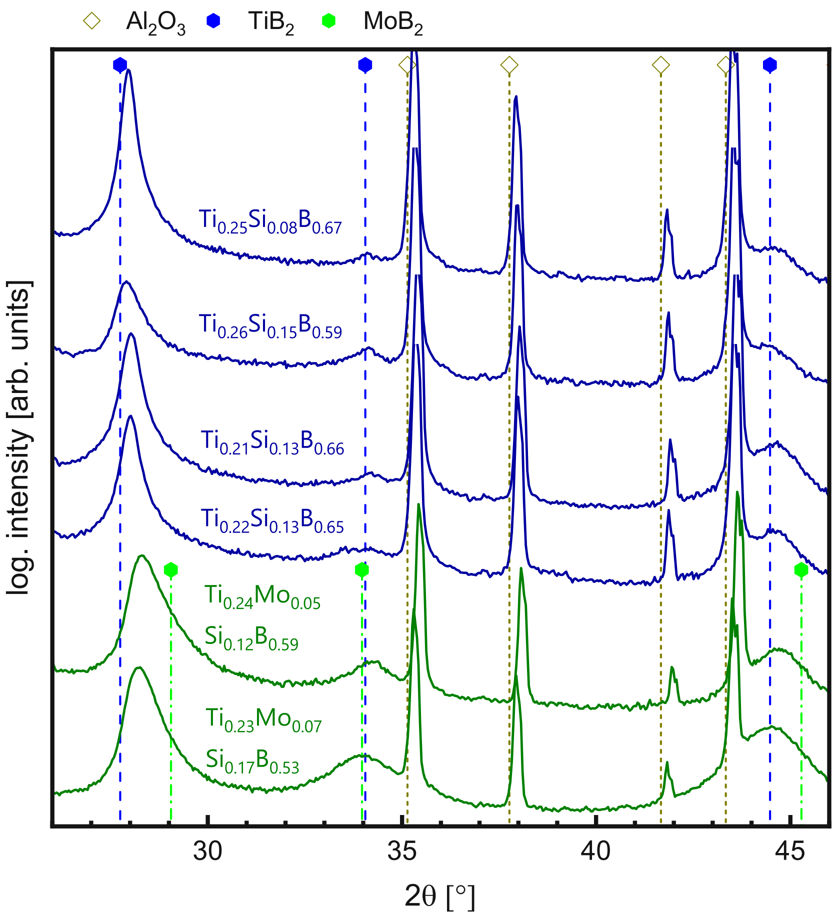

Figure 5.4: XRDs of DCMS deposited coatings from the targets listed in Table 4.1 in the as-deposited state

The X-ray diffractograms of the Ti-Mo-Si-B-based series of films deposited at various bias potentials are presented in Figure 5.5. The diffractograms of the coatings deposited with a bias voltage of -40 V, -80 V, -100 V, and -120 V appear very similar with a single hexagonal $Ti(Mo)B_2$ phase (peaks between the blue and green lines). The peak at $\sim$21° of the -40 V, -120 V, and -150 V coatings is assumed to be an artefact because it has not been present in other X-ray diffractograms on different substrates of the $Ti_{0.23}Mo_{0.07}Si_{0.17}B_{0.53}$ film (see Figure A.1 in the appendix). The -80 V film exhibits a broadened main peak at $\sim$28°. The $\sim$34° peak is the same size for the -80 V, -100 V, and -120 V coatings and a bit less intense than the one in the -40 V film. The same accounts for the $\sim$44.5° peak being the same intensity as the one at $\sim$34° for the -80 V, -100 V, and -120 V coatings. At -150 V, the peaks at $\sim$34° and $\sim$44° have changed in form and moved towards smaller 2Θ values. The peak intensity increase at $\sim$34 ° indicates a change in the preferred crystalline orientation from the (001) direction towards the (100) direction.

At -150 V, the peak at ∼28° slightly shifted towards lower 2Θ, with an additional peak at ∼24°. These changes suggest the separation of the single solid solution $Ti(Mo)B_2$ phase and the development of an additional phase of hexagonal MoB_4. This phase is plausible as the chemical analyses (Table 5.2 in 5.1.1 and Table A.2 in the appendix) depict a constant Mo-content in the films.

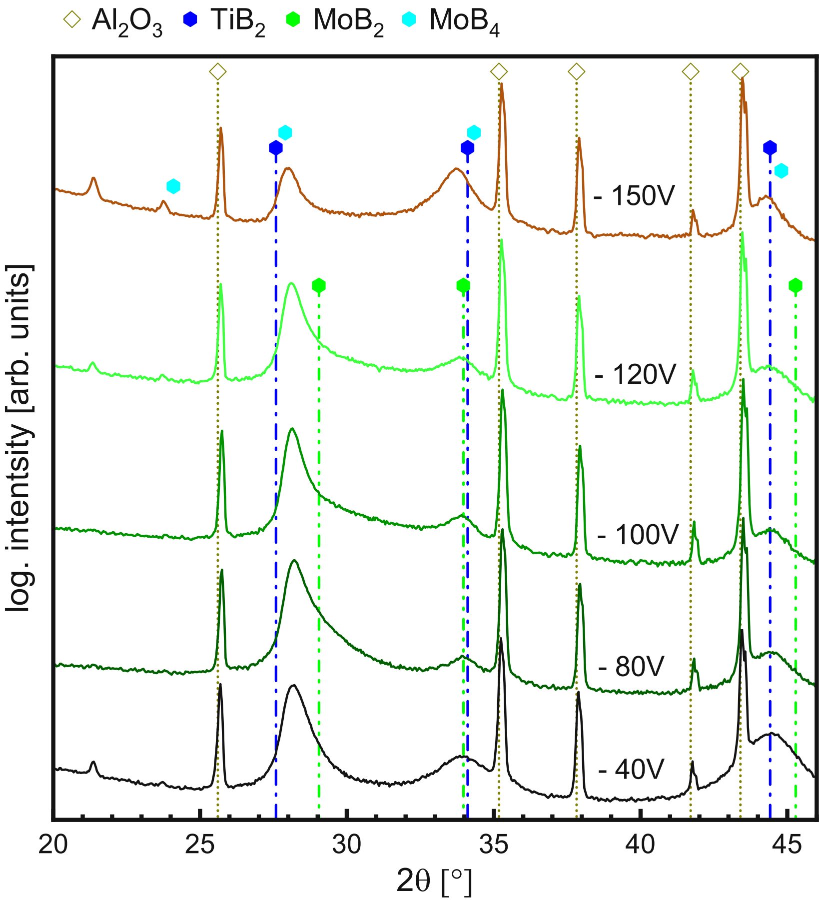

Figure 5.5: XRDs of the bias series deposited Ti-Mo-Si-B coatings sputtered from the $TiB_2/MoSi_2$ [80/20] target in the as-deposited state

Figure 5.6 depicts the X-ray diffractograms from the Ti-Mo-Si-B coatings deposited in the HIPIMS series compared to the DCMS deposited $Ti_{0.23}Mo_{0.07}Si_{0.17}B_{0.53}$ film. The peaks of all diffractograms indicate the presence of the single hexagonal $TiMoB_2$ phase. However, there is a peak intensity decrease at shorter pulse duty cycles. The intensity decline of the most prominent (001) TiB_2 peak at ∼28° indicates a less pronounced preferred crystalline orientation. Additionally, the gradual shift of the $TiMoB_2$ phase towards lower 2Θ may indicate a decrease in Mo within the solid solution phase or changed residual stresses within the films.

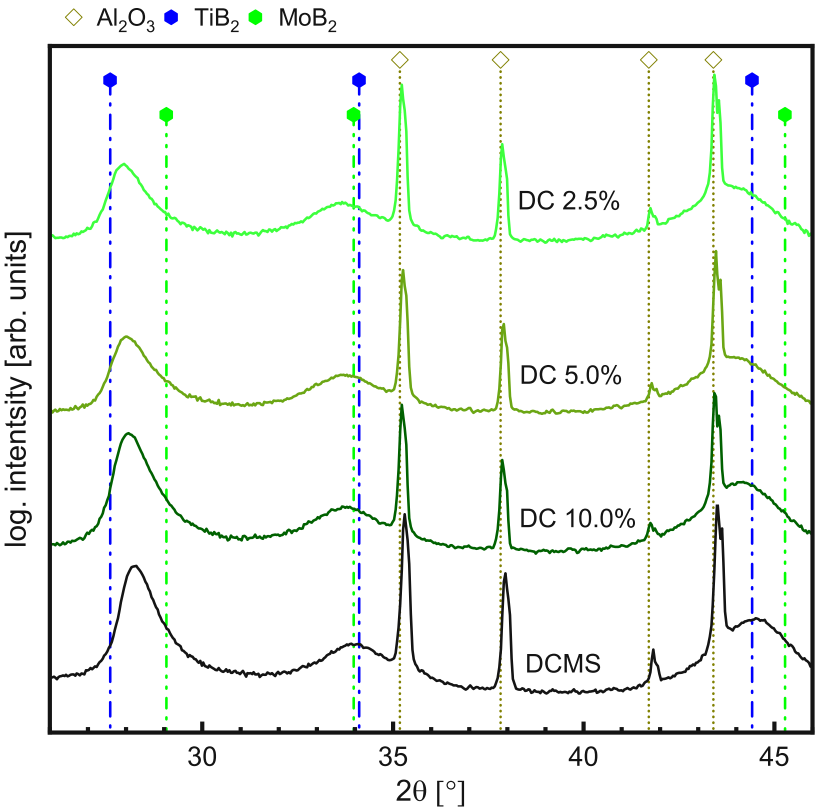

Figure 5.6: XRDs of HIPIMS-deposited coatings (at f = 1kHz) sputtered from the $TiB_2/MoSi_2$ [80/20] target in the as-deposited state.

5.1.4 Mechanical properties

Table 5.4 shows the elastic moduli and hardness values of the DCMS deposited coatings compared to un-alloyed binary $TiB_{2.57}$ (row 1 in Table 5.4) deposited on the same PVD system [113].

All alloyed TiB_2-based as-deposited coatings (rows 2 to 7 in Table 5.4) exhibit significantly decreased elastic moduli and hardness values compared to the $TiB_{2.57}$ film. Higher Si content decreases the measured mechanical properties of the ternary system. The highest elastic modulus and hardness values are achieved for the film composition $Ti_{0.25}Si_{0.08}B_{0.67}$ (row 2) followed by $Ti_{22}Si_{0.13}B_{0.65}$ (row 5), $Ti_{21}Si_{0.13}B_{0.66}$ (row 4) and $Ti_{0.26}Si_{0.15}B_{0.59}$ (row 3).

Moving to the quaternary Ti-Mo-Si-B system (rows 6 and 7 of Table 5.4), the $Ti_{0.24}Mo_{0.05}Si_{0.12}B_{0.59}$ film (row 6) depicts a higher elastic modulus and hardness than the $Ti_{0.23}Mo_{0.07}Si_{0.17}B_{0.53}$ film (row 7). Hence, the film with lower alloying content achieved higher values.

The hardness value (24.38 ±0.71 GPa) of the thoroughly investigated $Ti_{0.23}Mo_{0.07}Si_{0.17}B_{0.53}$ film is slightly below the achieved hardness of ∼25 GPa from Glechner et al. [28] for their $TiB_{2\pm z}$ with a 20 at. % Si content and from Navidi Kashani et al. [18] for their $(Ti_{0.34}Al_{0.66})B_{2.4}$

film. Furthermore, the elastic modulus (409.11 ±14.74 GPa) of the $Ti_{0.23}Mo_{0.07}Si_{0.17}B_{0.53}$ film is higher than the one from the $(Ti_{0.34}Al_{0.66})B_{2.4}$ film with ∼330 GPa [18].

Table 5.4: Elastic moduli and hardness values of as-deposited coatings

Film composition [at. %]	**Hardness [GPa]**	**Elastic Modulus [GPa]**	**Target composition [ratio]**
$TiB_{2.57}$ [28]	38.2 ±3.3	552.0 ±90.2	TiB_2 [100]
$Ti_{0.25}Si_{0.08}B_{0.67}$	30.53 ±0.92	448.77 ±12.89	$TiB_2/TiSi_2$ [90/10]
$Ti_{0.26}Si_{0.15}B_{0.59}$	23.76 ±0.54	401.11 ±15.23	$TiB_2/TiSi_2$ [80/20]
$Ti_{21}Si_{0.13}B_{0.66}$	24.10 ±0.78	402.20 ±10.30	$TiB_2/Ti_5Si_3/SiB_6$ [77.12/8.58/14.30]
$Ti_{22}Si_{0.13}B_{0.65}$	25.63 ±0.71	402.75 ±8.69	$TiB_2/Ti_5Si_3/SiB_6$ [58.89/15.44/25.67]
$Ti_{0.24}Mo_{0.05}Si_{0.12}B_{0.59}$	27.40 ±0.74	430.25 ±6.16	$TiB_2/MoSi_2$ [85/15]
$Ti_{0.23}Mo_{0.07}Si_{0.17}B_{0.53}$	24.38 ±0.71	409.11 ±14.74	$TiB_2/MoSi_2$ [80/20]

Figure 5.7 depicts the Ti-Mo-Si-B films' hardness and elastic modulus values deposited in the varying bias voltage series. The hardness values of the -40 V, -80 V, -100 V, and -120 V coatings show an alternating pattern ranging from ∼22.9 GPa (-80 V film) to ∼25.7 GPa (-100 V film). A similar behaviour is observed for the elastic modulus ranging from ∼386.4 GPa (-80 V film) to ∼417.8 GPa (-100 V film). The -150 V film shows a significant increase in hardness of ∼29.1 GPa and an elastic modulus of ∼469.7 GPa. This increase in hardness at the highest bias voltage of -150 V can be correlated to the previously reported low Si amount (∼6.5 at. %) for this coating (see Table 5.2).

Figure 5.8 depicts the influence of the pulse duty cycle on the hardness and E-modulus of Ti-Mo-Si-B coatings deposited by HIPIMS compared to a DCMS-deposited film. All the HIPIMS-deposited films show an increased hardness compared to the DCMS-deposited coating. The coatings deposited at a lower pulse duty cycle of 5 % and 2.5 % exhibit a similarly high hardness of ∼26.8 GPa and ∼26.5 GPa, respectively. Furthermore, the coatings deposited with 10 % and 5 % d.c. achieved the highest elastic moduli values of ∼432 GPa and ∼433 GPa, respectively. The 2.5 % duty cycle deposited film displayed a decrease in elastic modulus to ∼401 GPa, which is lower than the one obtained for the DCMS deposited coating.

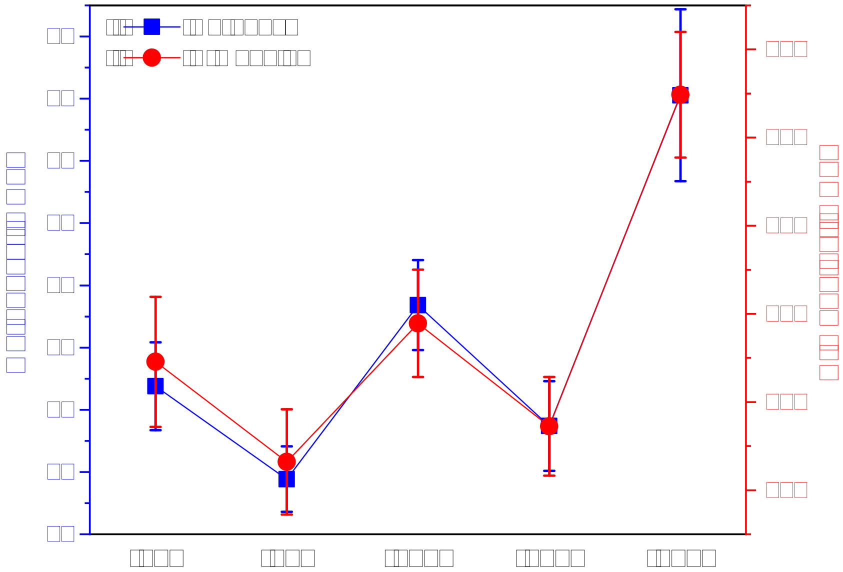

Figure 5.7: Elastic moduli and hardness values of the coatings sputtered at varied bias potentials from the TiB_2/$MoSi_2$ [80/20] target in the as-deposited state.

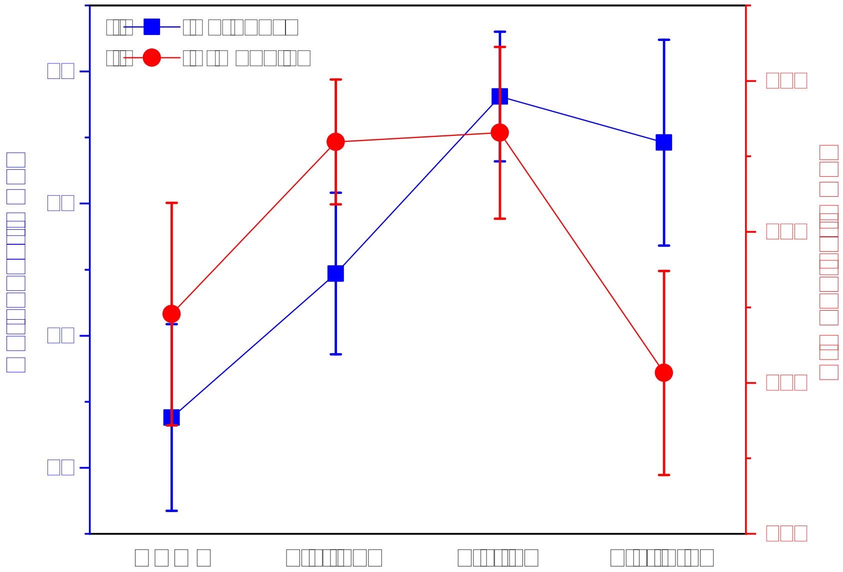

Figure 5.8: Elastic moduli and hardness values of HIPIMS-deposited coatings (at f = 1kHz) sputtered from the TiB_2/$MoSi_2$ [80/20] target at different pulse duty cycles in the as-deposited state.

5.2 Thermal analysis

5.2.1 Phase formation

Figure 5.9 shows X-ray diffractograms of the vacuum-annealed $Ti_{0.23}Mo_{0.07}Si_{0.17}B_{0.53}$ coating up to 1100 °C. Up to 600 °C, they exhibit only the peaks of the single hexagonal solid solution $TiMoB_2$. At 650 °C, a peak starts to evolve at 39.9°, indicating a growing tetragonal α-$MoSi_2$ phase, and a new 47.3° peak suggests the development of a cubic, elemental Si phase. The 57.4° peak narrows and shifts towards the TiB_2 peak at 56.95°. All these changes indicate the beginning of the phase decomposition of the single $TiMoB_2$ phase.

With increasing annealing temperature, up to 900 °C, the elemental Si and $MoSi_2$ peaks become more pronounced. New $MoSi_2$ peaks evolve at 29.9° (at 700 °C), 22.5° and 62.3° (at

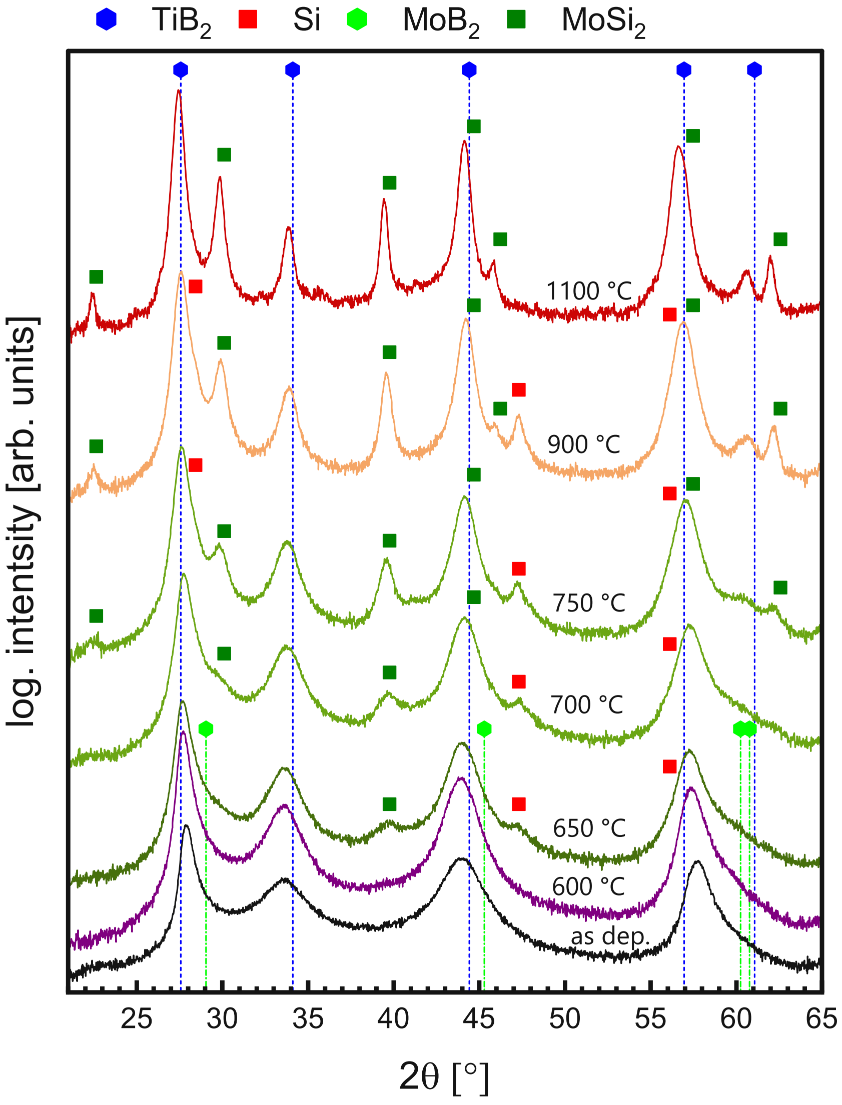

Figure 5.9: In-situ XRD of vacuum-annealed $Ti_{0.23}Mo_{0.07}Si_{0.17}B_{0.53}$ powder up to 1100 °C.

750 °C). Elemental Si also boosts the 47.2° peak as the peak broadens towards lower 2Θ at higher temperatures. At 900 °C, $MoSi_2$, with a new peak at 45.9°, and Si are equally at their intensity height. From 1050 °C to 1100 °C, the Si phase disappears as Mo diffuses into the intensifying $MoSi_2$ phase. Moreover, the TiB_2 phase remains dominant and intact throughout the annealing test.

5.2.2 High-temperature oxidation behaviour

Dynamic oxidation in synthetic air

Figure 5.10 shows the percentual mass changes during dynamic oxidation of the Ti(-Mo)-Si-$B_{2\pm z}$ coatings as a function of the annealing temperature. All the coatings exhibit an onset oxidation temperature of around 550 °C. The ternary Ti-Si-B-based films show similar behaviour with a steep mass increase and accelerated oxidation kinetics from 700 °C up to ~1100 °C. Following the initial mass increase, one observes a steep mass decrease as the volatile B_2O_3 evaporates. In contrast, the quaternary Ti-Mo-Si-B films display strong oxidation resistance and delayed oxidation kinetics compared to the ternary system, as the mass gain up to ~1100 °C is significantly lower. The coating with the higher Mo-Si content displays a flattened curve compared to the lower alloyed coating, with a mass plateau above 1100 °C. This behaviour with delayed oxidation kinetics indicates that the $Ti_{0.23}Mo_{0.07}Si_{0.17}B_{0.53}$ develops a highly protective oxide scale, which appears stable up to ~1340 °C.

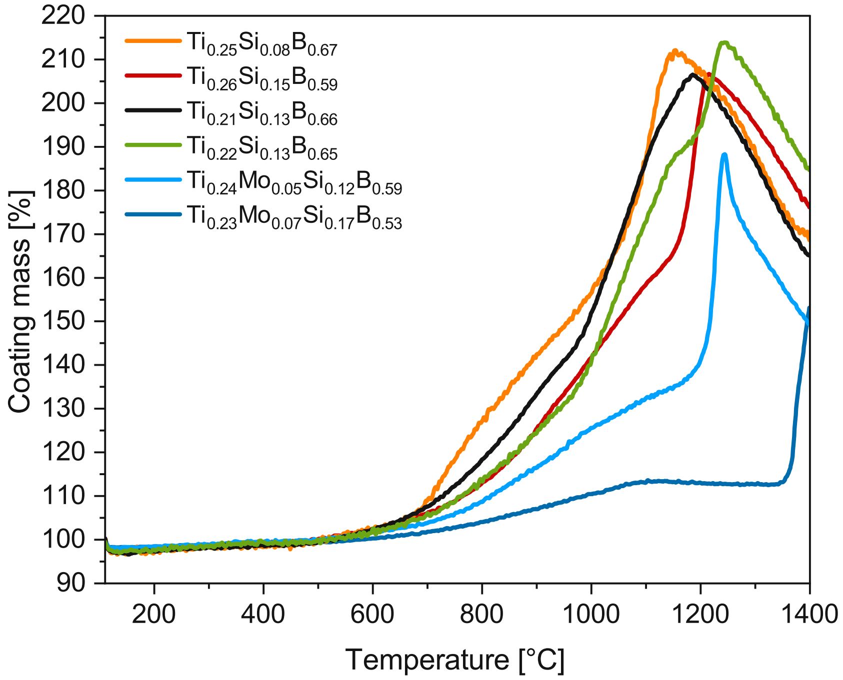

Figure 5.10: TG curves of mass change during dynamic oxidation measurement of DCMS deposited coatings in synthetic air up to 1400 °C.

Figure 5.11 displays the percentual mass gain of the Ti-Mo-Si-B films deposited with varying bias voltages. For all coatings, the onset oxidation temperature is around ~550 °C. At higher temperatures, all coatings of the bias series show increased mass gain and accelerated oxidation behaviour compared to the $Ti_{0.23}Mo_{0.07}Si_{0.17}B_{0.53}$ film deposited at -40 V. Between ~980 °C and ~1080 °C the samples exhibit a steep mass increase. The sample masses decrease drastically from ~1150 °C to ~1250 °C as volatile B_2O_3 evaporates.

Responsible for this accelerated oxidation behaviour at higher negative bias voltage could be the declined Si content (Table 5.2) and its distribution within the coatings. It is also possible that the increased B content within the coatings (Table 5.2) hinders the Si outward diffusion and formation of protective top scales.

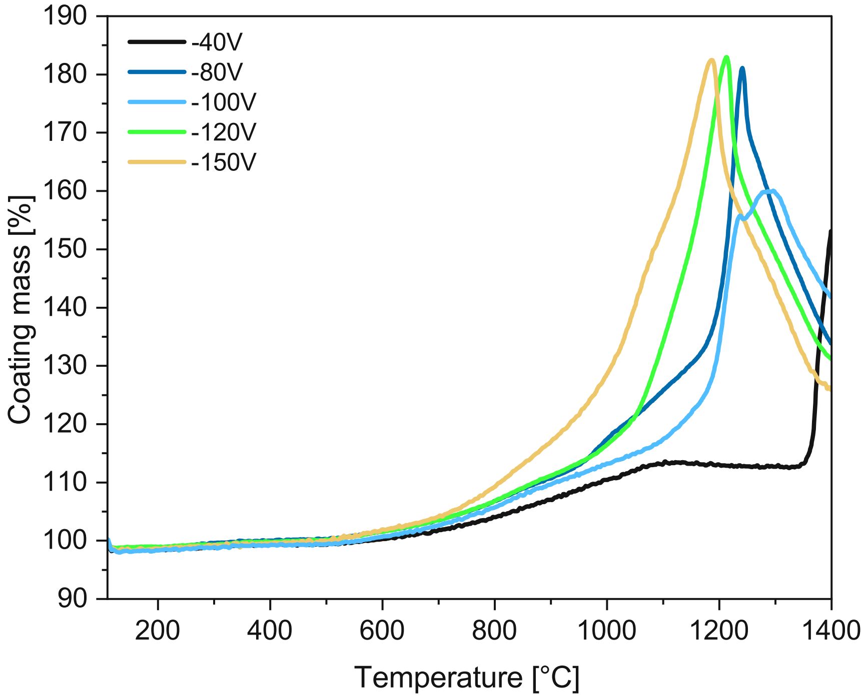

Figure 5.11: TG curves of mass change during dynamic oxidation measurement up to 1400 °C in synthetic air for the DCMS coatings sputtered from the $TiB_2/MoSi_2$ [80/20] target at varied bias potential.

Figure 5.12 depicts the dynamic oxidation curves of Ti-Mo-Si-B coatings deposited by HIPIMS. The HIPIMS-deposited coatings show the same onset oxidation temperature at ~550 °C and a very similar, low mass gain and oxidation rate compared to the DCMS-deposited $Ti_{0.23}Mo_{0.07}Si_{0.17}B_{0.53}$ coating. The film deposited with the 10 % pulse duty cycle reaches a mass plateau at about ~1000 °C indicating the formation of a protective oxide scale, which is stable until ~1300 °C. Above this temperature, the 10 % d.c. coating showed a very steep increase in mass up to ~1390 °C.

The coatings deposited with a 5 % and 2.5 % pulse duty cycle experience a steep mass increase and accelerated oxidation kinetics at ∼1150 °C. Over ∼1225 °C, the mass declines significantly, implying the evaporation of the volatile oxide B_2O_3. The accelerated oxidation kinetics may be influenced by the microstructure of the HIPIMS films with finer morphology altering the Si distribution and its diffusibility to form a protective oxide scale.

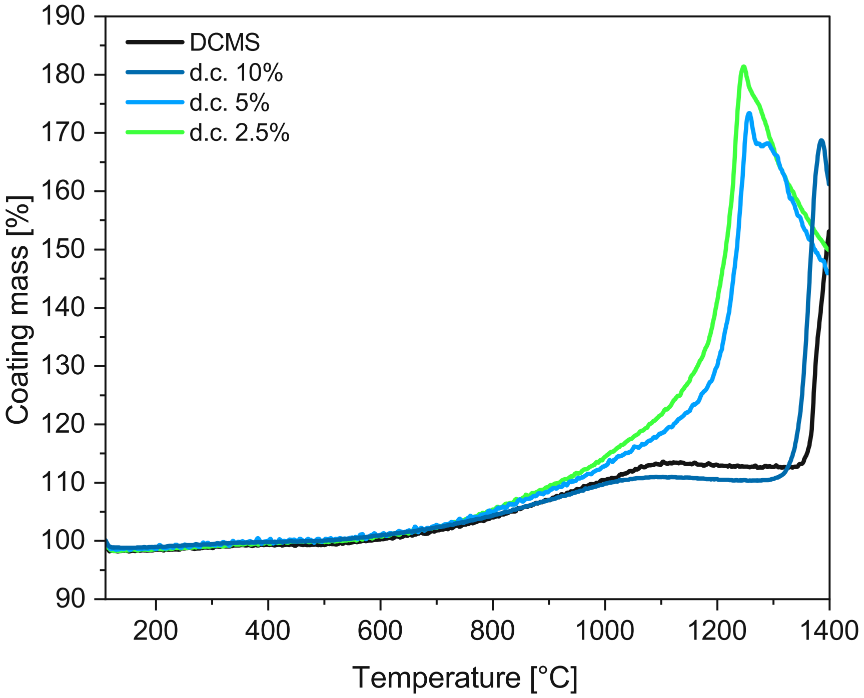

Figure 5.12: TG curves of the mass change during dynamic oxidation measurement up to 1400 °C in synthetic air for HIPIMS-deposited coatings sputtered from the $TiB_2/MoSi_2$ [80/20] target.

Isothermal oxidation in synthetic air

Figure 5.13 shows the mass gain during isothermal oxidation tests in synthetic air in the range of 700 °C to 1000 °C for two ternary Ti-Si-B films and in the range of 800 °C to 1200 °C for quaternary Ti-Mo-Si-B films. The percentual mass change is displayed as a function of the time and differs between the ternary Ti-Si-B coatings (100 % to 210 %, in Figure 5.13a and b) and the quaternary Ti-Mo-Si-B coatings (100 % to 140 %).

The $Ti_{0.25}Si_{0.08}B_{0.67}$ (Figure 5.13a) and $Ti_{0.26}Si_{0.15}B_{0.59}$ (Figure 5.13b) coatings developed similar behaviour, with the oxidation rates of the $Ti_{0.25}Si_{0.08}B_{0.67}$ coating (Figure 5.13a) being consistently higher due to the lower Si-alloying content (see chemical analysis in Subchapter 5.1.1). The isothermal measurements show increasingly parabolic oxidation kinetics at 700 °C to 900 °C, accelerating strongly at 1000 °C.

The $Ti_{0.24}Mo_{0.05}Si_{0.12}B_{0.59}$ film in Figure 5.13c displays parabolic oxidation kinetics at 800 °C, while the parabolic kinetics are accelerated at 900 °C. From 1000 °C, the oxidation kinetics turned to very low parabolic rates, with strongly delayed oxidation kinetics up to 1100 °C. At 1200 °C, after a steep initial mass gain, the oxidation rate decreases drastically after ∼2 min. After ∼20 min, the mass decreases slowly and reaches a plateau after ∼50 min indicating the formation of a highly protective oxide scale.

Figure 5.13d displays the oxidation kinetics of the $Ti_{0.23}Mo_{0.07}Si_{0.17}B_{0.53}$ film. At 800 °C, the coating exhibits a low linear oxidation rate. For the experiments at 900 °C, 1000 °C, and 1100 °C, no mass gain is visible throughout the test duration, indicating the development of the oxide scale with high protective capabilities. At 1200 °C, there is a sharp initial mass gain, followed by a plateau establishing after ∼1 min of oxidation time, which is a clear sign of the formation of a dense and highly protective oxide scale for $Ti_{0.23}Mo_{0.07}Si_{0.17}B_{0.53}$.

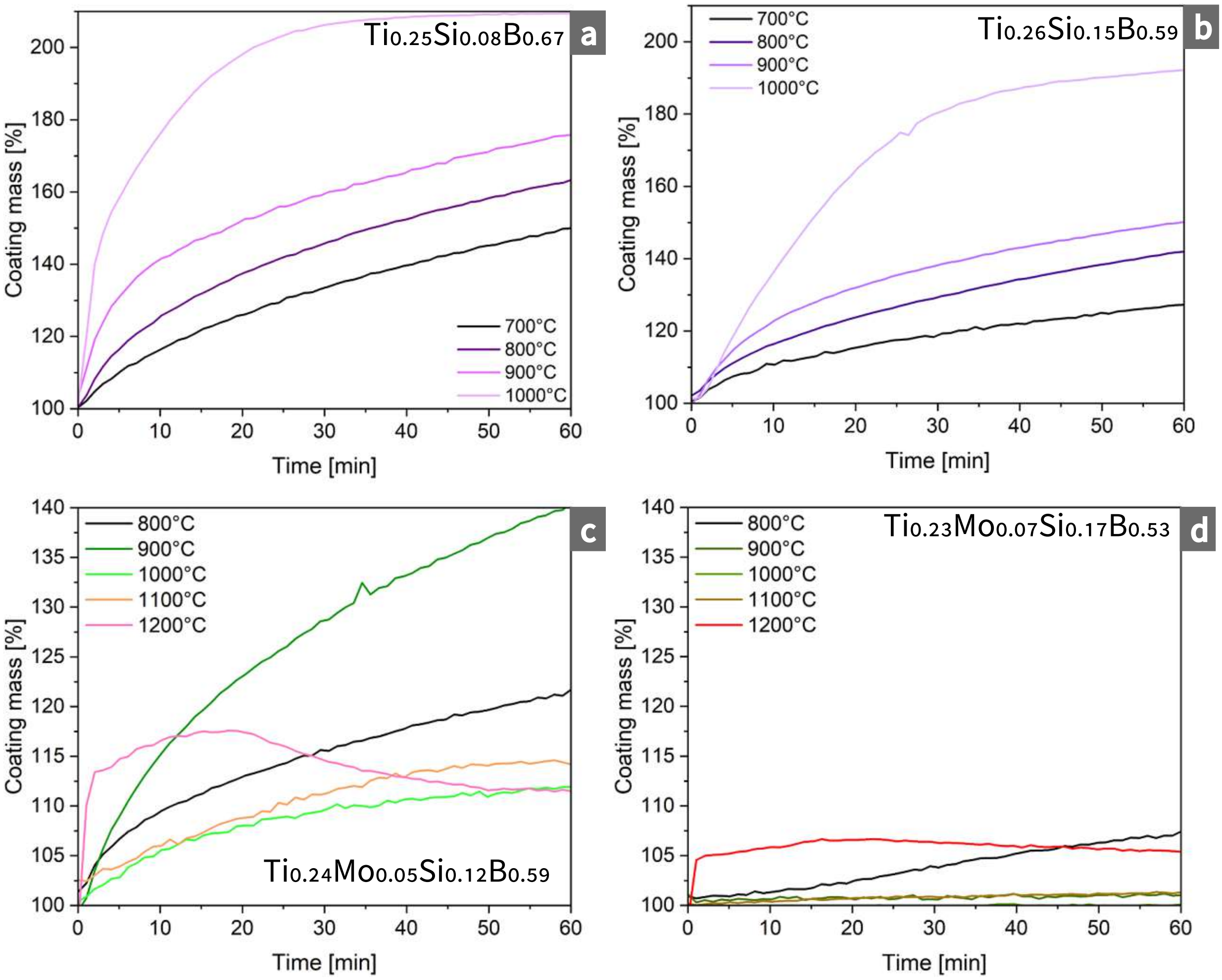

Figure 5.13: Mass gain during isothermal oxidation in synthetic air for 1 h at respective temperatures for (a) $Ti_{0.25}Si_{0.08}B_{0.67}$, (b) $Ti_{0.26}Si_{0.15}B_{0.59}$, (c) $Ti_{0.24}Mo_{0.05}Si_{0.12}B_{0.59}$, and (d) $Ti_{0.23}Mo_{0.07}Si_{0.17}B_{0.53}$ films on polycrystalline Al_2O_3 substrates.

Figure 5.14 depicts the X-ray diffractograms of the isothermally oxidised $Ti_{0.23}Mo_{0.07}Si_{0.17}B_{0.53}$ coatings, previously discussed in the last paragraph and shown in Figure 5.13d. For reference, the XRD of the as-deposited $Ti_{0.23}Mo_{0.07}Si_{0.17}B_{0.53}$ film is shown in black. Across the diffractograms of all temperatures, the peaks are shifted to higher 2Θ values by approximately 0.4 °.

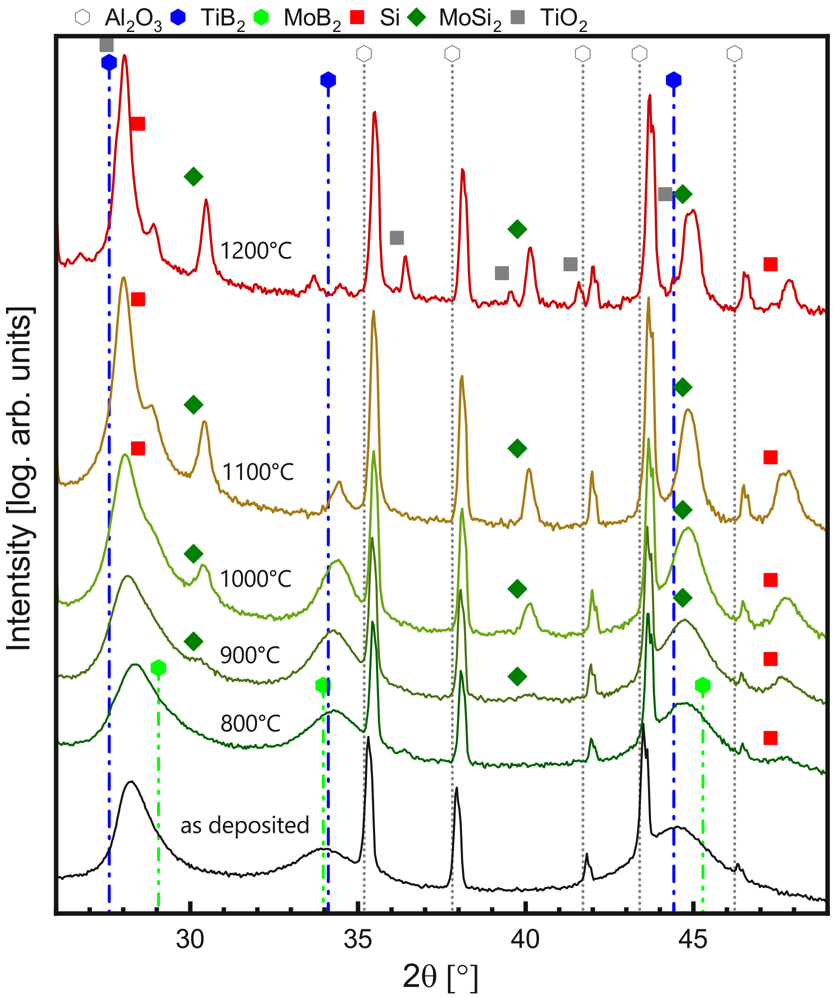

Figure 5.14: XRDs of $Ti_{0.23}Mo_{0.07}Si_{0.17}B_{0.53}$ films isothermally oxidised in synthetic air for 1 h.

At 800 °C, the diffractogram displays only the hexagonal $TiMoB_2$ peaks (discussed for the as-deposited film, see Subchapter 5.1.3), the substrate peaks (Al_2O_3), and a new peak building at ∼47.7° which is assigned to elemental, cubic Si. At 900 °C, $MoSi_2$ peaks start to form at ∼30.4°, and ∼40.1°. Moreover, the peak at ∼45° gets narrower and more intense, indicating another $MoSi_2$ peak overlapping with the TiB_2 peak. The forming $MoSi_2$ peaks indicate the outward diffusion of Mo from the solid solution $TiMoB_2$ phase described in the previous Subchapter (5.2.1). At 1000 °C, the $MoSi_2$ and Si peaks grow, and a shoulder develops at ∼28.9°, displaying another peak of the elemental Si phase. At 1100 °C, the $MoSi_2$ and Si peaks become more pronounced, followed by a decline of Si peaks at 1200 °C. At 1200 °C, new peaks arise at ∼36.4°, ∼39.5°, ∼41.6°, and ∼44.4°, indicating the formation of rutile TiO_2. At ∼27.8°, a change in the steepness of the intensity towards the ∼28° TiB_2 peak may indicate another TiO_2 peak. However, the hexagonal TiB_2 peaks are still the most dominant in the diffractogram proving the intactness of the coating. The peak at ∼33.7° could not be identified.

In Figure 5.15, all oxidised coatings developed a thin amorphous scale on top of the intact, unoxidised coating. The film thickness remains almost the same for the oxidations at all temperatures from 800 °C to 1200 °C (Figure 5.15b to e) compared to the as-deposited film (Figure 5.15a) due to the formation of highly protective dense scales. Within the unoxidised coating, the microstructure changes into globular morphology. The formation of globular grains with apparent grain coarsening indicates the recrystallisation of the coating material at higher temperatures above 1000 °C, confirming the XRD measurements' analyses (in Subchapter (5.2.1)) with the increased peak intensity of the hexagonal TiB_2 phase. The development of porosities could indicate the outward diffusion of Si and Mo.

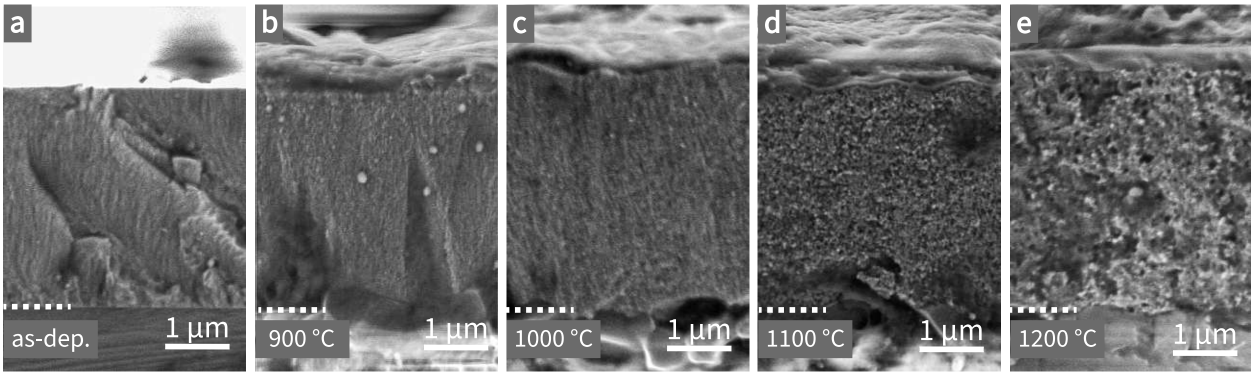

Figure 5.15: SEM cross-sections of $Ti_{0.23}Mo_{0.07}Si_{0.17}B_{0.53}$ coatings isothermally oxidised in synthetic air for 1 h: (a) as deposited, (b) oxidised at 900 °C, (c) oxidised at 1000 °C, (d) oxidised at 1100 °C, and (e) oxidised at 1200 °C;

Isothermal oxidation in ambient air

Figure 5.16a shows the TEM bright field (BF) view cross-section of an isothermally oxidised $Ti_{0.23}Mo_{0.07}Si_{0.17}B_{0.53}$ film on polycrystalline Al_2O_3 at 1000 °C in ambient air for 1 h. The protective W layer applied for the TEM sample preparation is visible on the top (bright-appearing). Beneath that is an amorphous dark-appearing thin scale on top of the unoxidised film. The film displays a globular morphology similar to the observations in the previous paragraph. Figure 5.16b contains the magnified section marked by the white dashed rectangle and the letter b in Figure 5.16a. The upper dashed line in the picture displays the interface between the top protective W layer applied during sample preparation and the amorphous scale, displayed in more detail: Some crystalline grains can be seen in the amorphous scale close to the scale-film interface marked by the lower dashed line. The film displays a thin sub-layer with a homogenous structure beneath the interface and a heterogenous globular morphology in the lower regions.

EELS mapping was used to identify the elemental composition in the c-h marked area in Figure 5.16b. Figure 5.16c displays the magnified DF image of the investigated spectrum area and d-h the elemental concentrations: The amorphous and highly protective top oxide scale is Si-O-based. Within the scale is one of the grains visible, which consist of Mo-Si-B. The homogenous structure near the scale-film interface is a mostly Si-depleted Ti-Mo-B section. In the lower half of the scan section: the unoxidised coating is mainly composed of TiB_2 with segregated regions enriched with elemental Si and $MoSi_2$ phases. The segregated Si and $MoSi_2$ phases confirm the in-situ XRD analyses (Figure 5.9), revealing a phase separation between the TiB_2-based matrix and Mo-Si at elevated temperatures. The presence of O within the film indicates some porosity.

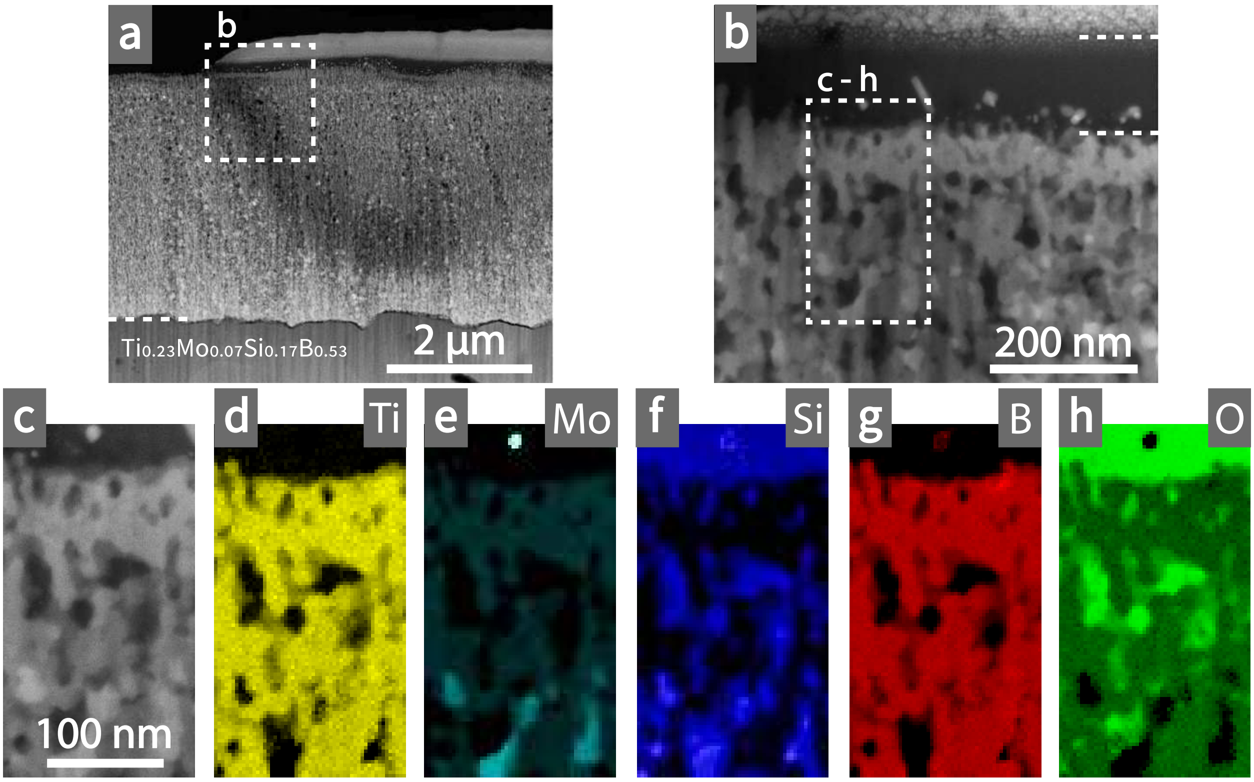

Figure 5.16: TEM cross-sectional analysis of 1 h isothermally oxidised $Ti_{0.23}Mo_{0.07}Si_{0.17}B_{0.53}$ films at 1000 °C in ambient air (a). (b) is the magnification of the section indicated by the dashed rectangle marked b in (a). The details marked in (b) indicate the EELS scan section in (c). In (d-h), the spectrum area of the analysis is marked, where brighter colours indicate a higher element concentration of Ti (d), Mo (e), Si (f), B (g), and O (h);

Figure 5.17a shows the cross-sectional TEM analysis of the $Ti_{0.23}Mo_{0.07}Si_{0.17}B_{0.53}$ coating oxidised at 1200 °C. The top protective W layer (dark grey) was applied during sample preparation. A dense amorphous, highly protective oxide scale (homogenous grey) is visible underneath. The intact coating exhibits globular morphology with more pronounced grain coarsening due to recrystallisation compared to the one oxidised at 1000 °C (Figure 5.16a). Figure 5.17b shows the magnification of the marked area labelled with b in Figure 5.17a: The magnification of the substrate-coating interface shows no reaction or interaction between the coating and the substrate nor delamination of the coating. In Figure 5.17c (magnification of the marked area labelled c in Figure 5.17a), small globular, crystalline grains are visible near the scale-coating interface within the scale.

Figure 5.17e contains the selected area electron diffraction (SAED) analysis of the circled area in Figure 5.17d (magnification of the dashed are labelled d in Figure 5.17a). The SAED shows no reflection at all, proving the amorphous character of the scale. The scan section of the EELS measurement in Figure 5.17f shows a dark field (DF) image of the area marked

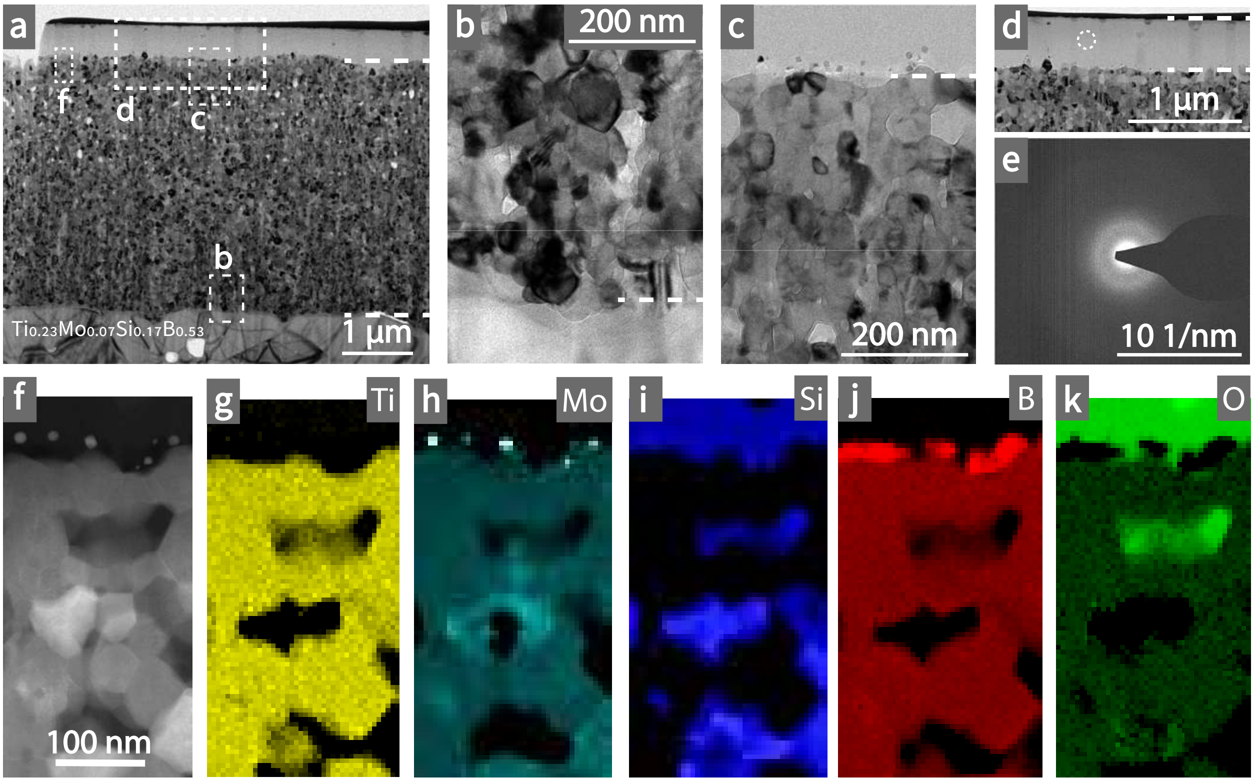

Figure 5.17: (a) shows the TEM cross-section of 1h isothermally oxidised $Ti_{0.23}Mo_{0.07}Si_{0.17}B_{0.53}$ film on polycrystalline Al_2O_3 in ambient air at 1200 °C with marked areas referring to the magnification with the respective letter. (b) depicts the view of the coating near substrate; In (c), the scale on top of the film is visible, whereas (d) shows the selected area for electron diffraction seen in (e). In (f), the spectrum area of the EELS analysis as seen in the TEM: brighter colours indicate a higher element concentration of Ti (g), Mo (h), Si (i), B (j), and O (k);

f in Figure 5.17a. The amorphous, highly protective oxide scale is mainly composed of Si-O, with no boron content confirming the analysis for the 1000 °C sample, suggesting an amorphous SiO_2 phase. This highly protective and dense oxide scale is responsible for outstanding oxidation resistance, as it exhibits a pronounced structural tolerance due to its glassy character. At the same time, it allows selective outward diffusion (e.g. for SiO) to prevent growing interfacial vapour pressure. [64] At the scale-film interface, the high B and Mo concentration could have resulted due to a mechanism described previously by Silvestroni et al. [121], where B_2O_3, trapped under the protective SiO_2 scale, reacts with $MoSi_2$ creating SiO_2 and MoB. The low amount of MoB may be responsible for the absence of MoB peaks in the X-ray diffractograms.

The intact, unoxidised coating is TiB_2 dominated with residual Mo in a solid solution. Grains of elemental Si are likely to be surrounded by $MoSi_2$ grains, indicating an ongoing Mo diffusion and reaction with Si. Such behaviour is likely as the Si phase in the XRD disappears and the intensity of $MoSi_2$ increases at 1100 °C during the in-situ vacuum annealing experiment of this coating (see Figure 5.9). The high O-concentration at the upper centre of the scan section hints towards a porous character of the coating.

Long-time oxidation tests

Figure 5.18 shows cross-sections of the long-time oxidised $Ti_{0.23}Mo_{0.07}Si_{0.17}B_{0.53}$ coatings at 1200 °C in ambient air. The films remained intact for up to 60 h. On the very top, the bright-appearing FIB-deposited protective layer applied in the preparation step before the milling of the samples can be seen. The oxide scales are dense and appear thicker than in the cross-sections of 1 h oxidised samples (Figure 5.15). In Figure 5.18a, the top scale is amorphous with some randomly distributed crystallites that could be crystallised SiO_2 identified in the X-ray diffractogram at 1200 °C during an in-situ XRD measurement in ambient air (Figure A.2 in the appendix). A few crystallites are still visible within the amorphous scale in the 10 h sample. However, the scale appears completely amorphous after 30 h and 60 h.

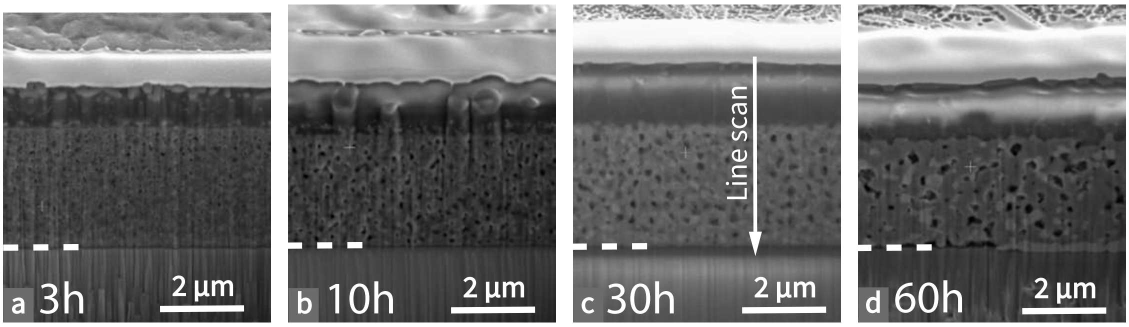

Figure 5.18: FIB cross sections of $Ti_{0.23}Mo_{0.07}Si_{0.17}B_{0.53}$ coatings on sapphire substrates oxidised in ambient air at 1200 °C for: (a) 3 h, (b) 10 h, (c) 30 h, and (d) 60 h;

In all cross-sections in Figure 5.18, the film thickness remains almost constant, and porosity is visible. Additionally, the microstructure depicts the same globular morphology that experiences grain coarsening over time due to recrystallisation processes. The coating oxidised for 60 h remains intact, but exhibits grown pores with high porosity at the film-substrate interface (Figure 5.18d).

The arrow in Figure 5.18c indicates the direction of the EDX line scan analysed in Figure 5.19 for the $Ti_{0.23}Mo_{0.07}Si_{0.17}B_{0.53}$ film air-annealed at 1200 °C for 30 h. The EDX line scan analysis depicts the elemental composition along the cross-section. However, the B amount in the EDX analysis is inaccurate and, therefore, is not considered. The elemental analysis proves that the amorphous, dense, highly protective oxide scale is nearly stoichiometric SiO_2. Crossing the scale-film interface along the x-axis, one does not see a substantial depletion of either Ti, Mo, or Si, confirming the film's intactness after 30 h at 1200 °C. The film-substrate interface is visible as the surging O content indicates the single crystalline sapphire (Al_2O_3) substrate.

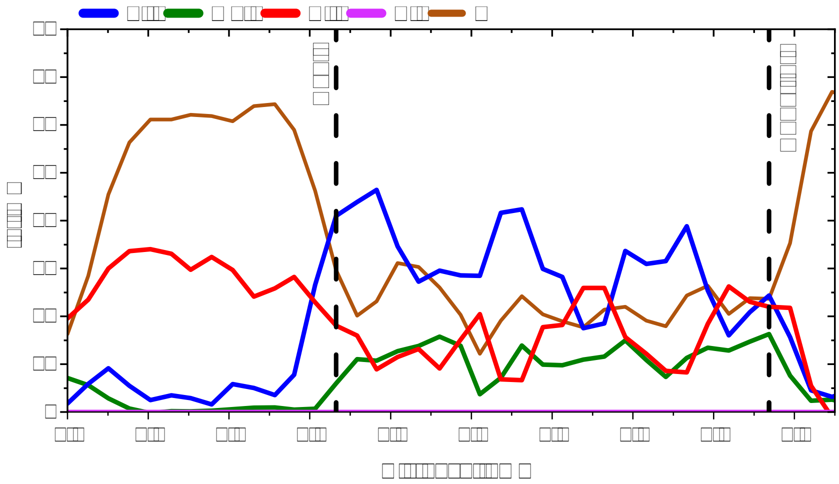

Figure 5.19: EDX line scan (indicated in Figure 5.18c) of a 30 h at 1200 °C oxidised $Ti_{0.23}Mo_{0.07}Si_{0.17}B_{0.53}$ film deposited on a sapphire substrate.

CHAPTER 6

Conclusions

In this work, ternary Ti-Si-$B_{2\pm z}$ and quaternary Ti-Mo-Si-$B_{2\pm z}$ coatings have been deposited from alloyed TiB_2/$TMSi_2$ compound targets to study their oxidation resistance, phase formation and mechanical properties.

All the Ti-Si-$B_{2\pm z}$ films displayed a crystalline structure with a single hexagonal TiB_2 phase (space group 191) and a preferred (001) orientation. The quaternary Ti-Mo-Si-$B_{2\pm z}$ films showed broadened peaks of the single solid solution hexagonal Ti(Mo)B_2 phase. No separate Si-based phase was identified in any of the grown coatings, indicating the dissolution of Si in the AlB_2-structure or its segregation as an amorphous phase at the grain boundaries. The measured mechanical properties of the alloyed coatings in terms of hardness and elastic modulus decreased with increasing Si and Mo alloying content. The elastic moduli and hardness values ranged from ~401 GPa to ~449 GPa, from ~23.8 GPa to ~30.5 GPa for ternary Ti-Si-B films, and from ~409 GPa to ~430 GPa and from ~24.4 GPa to ~27.4 GPa for the quaternary Ti-Mo-Si-B system.

Isothermal and dynamic oxidation tests up to 1400 °C revealed superior oxidation resistance of the quaternary Ti-Mo-Si-$B_{2\pm z}$ coatings compared to their ternary counterparts. The ternary Ti-Si-$B_{2\pm z}$ films showed a steep mass increase and accelerated oxidation kinetics above the oxidation onset temperature of 550 °C. They exhibited parabolic oxidation kinetics in isothermal oxidation experiments between 700 °C and 1000 °C, whereas the quaternary Ti-Mo-Si-$B_{2\pm z}$ coatings exhibited high-temperature oxidation resistance with retarded oxidation kinetics up to ~1340 °C. By increasing the Mo-Si content, the slope of the dynamic mass curve reduced and exhibited a plateau over 1000 °C due to the formation of a highly protective oxide scale.

The $Ti_{0.23}Mo_{0.07}Si_{0.17}B_{0.53}$ preserved an outstanding oxidation resistance with retarded oxidation kinetics up to 60 h at 1200 °C on account of the formation of a thin amorphous, dense and protective SiO_2 oxide scale on top. A beneficial phase separation of $MoSi_2$ and TiB_2

occurring at around 650 °C boosts the high temperature oxidation resistance by facilitating the formation of SiO_2 protective scale through the selective oxidation of Si and suppressing the formation of the volatile B_2O_3 phase.

Furthermore, two series of Ti-Mo-Si-$B_{2\pm z}$ coatings were deposited using HIPIMS and DCMS at varied substrate bias voltage to enhance the mechanical properties in relation to the high-temperature oxidation resistance. The increase of substrate bias potential resulted in an increase in hardness and elastic modulus of ∼29 GPa and ∼470 GPa, respectively. However, these improvements came with the deterioration of oxidation resistance. Furthermore, the HIPIMS coatings exhibited a maximum increased hardness and elastic modulus of ∼26.8 GPa and ∼433 GPa, respectively and a similar loss in oxidation resistance except for the coating deposited with a 10 % d.c.. This film displayed an increased elastic modulus (∼432 GPa) and hardness (∼25.5 GPa) while retaining the outstanding oxidation resistance.

In summary, alloying $TiB_{2\pm z}$ coatings with secondary disilicide-based phases offers a promising route to significantly enhance the high-temperature oxidation resistance while maintaining good mechanical properties. This work demonstrates the high potential of quaternary Ti-Mo-Si-$B_{2\pm z}$ coatings in high-temperature applications based on their outstanding high-temperature oxidation resistance and reasonable mechanical properties.

Bibliography

[1] J. Riskin and A. Khentov, in *Electrocorrosion Prot. Met.* (Elsevier, 2019) pp. 3–47.

[2] D. J. Young, *High Temp. Oxid. Corros. Met. Second Ed.* (Elsevier, 2016) pp. 1–733.

[3] M. J. Schofield, in *Plant Eng. Ref. B.* (Elsevier, 2002) pp. 33–1–33–25.

[4] R. Javaherdashti, Anti-Corrosion Methods Mater. **47**, 30 (2000).

[5] G. Koch, in *Trends Oil Gas Corros. Res. Technol.* (Elsevier, 2017) pp. 3–30.

[6] Y. Hu, T. Cao, C. Cheng, L. Zhang, and J. Zhao, Appl. Surf. Sci. **484**, 209 (2019).

[7] J. Wang, H. Xue, and Y. Wang, Rare Met. **40**, 616 (2021).

[8] M. Li, P. Wang, Y.-Q. Yang, Y.-Z. Yang, H.-Q. Pei, Z.-X. Wen, and Z.-F. Yue, J. Mater. Sci. **57**, 3822 (2022).

[9] L. Quintino, in *Surf. Modif. by Solid State Process.* (Elsevier, 2014) pp. 1–24.

[10] W. G. Fahrenholtz and G. E. Hilmas, Scr. Mater. **129**, 94 (2017).

[11] B. R. Golla, A. Mukhopadhyay, B. Basu, and S. K. Thimmappa, Prog. Mater. Sci. **111**, 100651 (2020).

[12] M. Magnuson, L. Hultman, and H. Högberg, Vacuum **196**, 110567 (2022).

[13] P. H. Mayrhofer, C. Mitterer, and H. Clemens, Adv. Eng. Mater. **7**, 1071 (2005).

[14] F. Kunc, J. Musil, P. H. Mayrhofer, and C. Mitterer, Surf. Coatings Technol. **174-175**, 744 (2003).

[15] X. Cai, S. Ding, K. Wen, L. Xu, H. Xue, S. Xin, and T. Shen, J. Eur. Ceram. Soc. **41**, 5100 (2021).

[16] T. Parthasarathy, R. Rapp, M. Opeka, and R. Kerans, Acta Mater. **55**, 5999 (2007).

[17] Y. H. Koh, S. Y. Lee, and H. E. Kim, J. Am. Ceram. Soc. **84**, 239 (2001).

[18] A. H. Navidi Kashani, S. Mráz, D. M. Holzapfel, M. Hans, L. Löfler, P. Ondračka, D. Primetzhofer, and J. M. Schneider, Surf. Coatings Technol. **442**, 128190 (2022).

[19] S. Dorri, J. Palisaitis, G. Greczynski, I. Petrov, J. Birch, L. Hultman, and B. Bakhit, Corros. Sci. **206**, 110493 (2022).

[20] M. Hasegawa, in *Treatise Process Metall.*, Vol. 1 (Elsevier, 2014) pp. 507–516.

[21] W. G. Fahrenholtz, E. J. Wuchina, W. E. Lee, and Y. Zhou, *Ultra-High Temp. Ceram. Mater. Extrem. Environ. Appl.*, edited by W. G. Fahrenholtz, E. J. Wuchina, W. E. Lee, and Y. Zhou, Vol. 9781118700 (Wiley, 2014) pp. 316–360.

[22] W. G. Fahrenholtz and G. E. Hilmas, Int. Mater. Rev. **57**, 61 (2012).

[23] A. Pugach, I. Golovko, and L. V. Dvorina, Sov. Powder Metall. Met. Ceram. **16**, 108 (1977).

[24] D. S. King, W. G. Fahrenholtz, and G. E. Hilmas, J. Eur. Ceram. Soc. **33**, 2943 (2013).

[25] A. Mukhopadhyay, G. B. Raju, B. Basu, and A. K. Suri, J. Eur. Ceram. Soc. **29**, 505 (2009).

[26] G. B. Raju, A. Mukhopadhyay, K. Biswas, and B. Basu, Scr. Mater. **61**, 674 (2009).

[27] G. B. Raju, B. Basu, N. H. Tak, and S. J. Cho, J. Eur. Ceram. Soc. **29**, 2119 (2009).

[28] T. Glechner, H. Oemer, T. Wojcik, M. Weiss, A. Limbeck, J. Ramm, P. Polcik, and H. Riedl, Surf. Coatings Technol. **434**, 128178 (2022).

[29] B. Grančič, M. Mikula, T. Roch, P. Zeman, L. Satrapinskyy, M. Gregor, T. Plecenik, E. Dobročka, Z. Hájovská, M. Mičušík, A. Šatka, M. Zahoran, A. Plecenik, and P. Kúš, Surf. Coatings Technol. **240**, 48 (2014).

[30] W. G. Fahrenholtz, G. E. Hilmas, I. G. Talmy, and J. A. Zaykoski, J. Am. Ceram. Soc. **90**, 1347 (2007).

[31] G. Akopov, M. T. Yeung, and R. B. Kaner, Adv. Mater. **29**, 1604506 (2017).

[32] D. Ni, Y. Cheng, J. Zhang, J.-X. Liu, J. Zou, B. Chen, H. Wu, H. Li, S. Dong, J. Han, X. Zhang, Q. Fu, and G.-J. Zhang, J. Adv. Ceram. **11**, 1 (2022).

[33] G. Raju and B. Basu, Key Eng. Mater. **395**, 89 (2008).

[34] Springer, "https://materials.springer.com/isp/crystallographic/docs/sd_1605612 (accessed on 2022-10-25)," (2022).

[35] R. G. Munro, J. Res. Natl. Inst. Stand. Technol. **105**, 709 (2000).

[36] H. Holleck, J. Vac. Sci. Technol. A Vacuum, Surfaces, Film. **4**, 2661 (1986).

[37] Y. Liu, L. St-Pierre, N. Fleck, V. Deshpande, and A. Srivastava, J. Mech. Phys. Solids **143**, 104060 (2020).

[38] N. Kalfagiannis, G. Volonakis, L. Tsetseris, and S. Logothetidis, J. Phys. D. Appl. Phys. **44**, 385402 (2011).

[39] M. Berger, L. Karlsson, M. Larsson, and S. Hogmark, Thin Solid Films **401**, 179 (2001).

[40] C. Fuger, R. Hahn, A. Hirle, P. Kutrowatz, M. Weiss, A. Limbeck, O. Hunold, P. Polcik, and H. Riedl, Surf. Coatings Technol. **446**, 128806 (2022).

[41] J. Thörnberg, B. Bakhit, J. Palisaitis, N. Hellgren, L. Hultman, G. Greczynski, P. O. Persson, I. Petrov, and J. Rosen, Surf. Coatings Technol. **420**, 127353 (2021).

[42] J. Schiøtz, F. D. Di Tolla, and K. W. Jacobsen, Nature **391**, 561 (1998).

[43] I. N. Remediakis, G. Kopidakis, and P. C. Kelires, Acta Mater. **56**, 5340 (2008).

[44] P. H. Mayrhofer, C. Mitterer, J. G. Wen, J. E. Greene, and I. Petrov, Appl. Phys. Lett. **86**, 131909 (2005).

[45] J. Thörnberg, J. Palisaitis, N. Hellgren, F. F. Klimashin, N. Ghafoor, I. Zhirkov, C. Azina, J. L. Battaglia, A. Kusiak, M. A. Sortica, J. E. Greene, L. Hultman, I. Petrov, P. O. Persson, and J. Rosen, Surf. Coatings Technol. **404**, 126537 (2020).

[46] J. Palisaitis, M. Dahlqvist, A. J. Hall, J. Thörnberg, I. Persson, N. Nedfors, L. Hultman, J. Greene, I. Petrov, J. Rosen, and P. O. Persson, Acta Mater. **204**, 116510 (2021).

[47] I. Zyganitidis, N. Kalfagiannis, and S. Logothetidis, Mater. Sci. Eng. B **165**, 198 (2009).

[48] R. Wiedemann, H. Oettel, and M. Jerenz, Surf. Coatings Technol. **97**, 313 (1997).

[49] M. G. Fontana, Corrosion **19**, 199t (1963).

[50] N. Birks, G. H. Meier, and F. S. Pettit, *Introd. to High Temp. Oxid. Met. Second Ed.*, Vol. 9780521480 (Cambridge University Press, 2006) pp. 1–338.

[51] O. Kubaschewski and B. E. Hopkins, Mater. Corros. und Korrosion **5**, 477 (1954).

[52] A. Tampieri and A. Bellosi, J. Mater. Sci. **28**, 649 (1993).

[53] A. Münster and G. Schlamp, Zeitschrift fur Phys. Chemie **25**, 116 (1960).

[54] V. B. Voitovich, V. A. Lavrenko, and V. M. Adejev, Oxid. Met. **42**, 145 (1994).

[55] A. Kulpa and T. Troczynski, J. Am. Ceram. Soc. **79**, 518 (1996).

[56] A. Münster, Zeitschrift für Elektrochemie, Berichte der Bunsengesellschaft für Phys. Chemie **63**, 807 (1959).

[57] R. Irving and I. Worsley, J. Less Common Met. **16**, 103 (1968).

[58] M. G. Barandika, J. J. Echeberría, J. M. Sánchez, and F. Castro, J. Mater. Chem. **8**, 1851 (1998).

[59] B. Basu, G. B. Raju, and A. K. Suri, Int. Mater. Rev. **51**, 352 (2006).

[60] G. Raju and B. Basu, Key Eng. Mater. **395**, 89 (2008).

[61] R. Viswanathan, T. S. L. Narasimhan, and S. Nalini, J. Phys. Chem. B **113**, 8362 (2009).

[62] C. Huber, S. Setoodeh Jahromy, C. Jordan, M. Schreiner, M. Harasek, A. Werner, and F. Winter, Energies **12**, 1086 (2019).

[63] B. Bakhit, J. Palisaitis, J. Thörnberg, J. Rosen, P. O. Persson, L. Hultman, I. Petrov, J. Greene, and G. Greczynski, Acta Mater. **196**, 677 (2020).

[64] M. M. Opeka, I. G. Talmy, and J. A. Zaykoski, J. Mater. Sci. **39**, 5887 (2004).

[65] H. Blom, T. Larsson, S. Berg, and M. Östling, J. Vac. Sci. Technol. A Vacuum, Surfaces, Film. **7**, 162 (1989).

[66] T. Larsson, H.-O. Blom, S. Berg, and M. Östling, Thin Solid Films **172**, 133 (1989).

[67] X. Cao, B. Wang, X. Ma, L. Feng, X. Shen, and C. Wang, Ceram. Int. **47**, 9881 (2021).

[68] T. Murthy, J. Sonber, C. Subramanian, R. Fotedar, S. Kumar, M. Gonal, and A. Suri, Int. J. Refract. Met. Hard Mater. **28**, 529 (2010).

[69] T. Murthy, J. Sonber, C. Subramanian, R. Hubli, and A. Suri, Int. J. Refract. Met. Hard Mater. **33**, 10 (2012).

[70] B. Ramesh, E. Showman, S. A. M. Abraar, K. K. Saxena, M. Y. Tharwan, N. Alsaadi, S. Al Sofyani, and A. H. Elsheikh, Materials (Basel). **15**, 7096 (2022).

[71] A. Tampieri, E. Landi, and A. Bellosi, J. Therm. Anal. **38**, 2657 (1992).

[72] S. Cho, I. Jo, Y.-H. Lee, Y. W. Yoo, E. Byon, S.-K. Lee, and S.-B. Lee, Appl. Surf. Sci. **448**, 407 (2018).

[73] J. Cook, A. Khan, E. Lee, and R. Mahapatra, Mater. Sci. Eng. A **155**, 183 (1992).

[74] C. D. Wirkus and D. R. Wilder, J. Am. Ceram. Soc. **49**, 173 (1966).

[75] R. W. Bartlett, J. W. McCamont, and P. R. Gage, J. Am. Ceram. Soc. **48**, 551 (1965).

[76] T. Murthy, R. Balasubramaniam, B. Basu, A. Suri, and M. Mungole, J. Eur. Ceram. Soc. **26**, 187 (2006).

[77] G. B. Raju, B. Basu, and A. K. Suri, J. Am. Ceram. Soc. **91**, 3320 (2008).

[78] T. Murthy, C. Subramanian, R. Fotedar, M. Gonal, P. Sengupta, S. Kumar, and A. Suri, Int. J. Refract. Met. Hard Mater. **27**, 629 (2009).

[79] G. Sade and J. Pelleg, MRS Proc. **402**, 131 (1995).

[80] G. Sade and J. Pelleg, Microelectron. Eng. **37-38**, 535 (1997).

[81] Y. M. Bilobrov, V. V. Trachevskii, A. A. Bondar, T. Y. Velikanova, L. V. Artyukh, V. Y. Pashchenko, and V. B. Soboliev, J. Phase Equilibria Diffus. **35**, 406 (2014).

[82] J.-I. Matsushita, T. Satsukawa, N. Iwamoto, X. L. Wang, J. F. Yang, T. Goto, T. Sekino, X. Y. Wu, S. Yin, and T. Sato, Mater. Sci. Forum **868**, 38 (2016).

[83] J. Neidhardt, S. Mráz, J. M. Schneider, E. Strub, W. Bohne, B. Liedke, W. Möller, and C. Mitterer, J. Appl. Phys. **104**, 063304 (2008).

[84] C. Mitterer, J. Solid State Chem. **133**, 279 (1997).

[85] M. Ohring, *Materials Science of Thin Films*, 3rd ed. (Elsevier, San Diego, Calif. [u.a.], 2002).

[86] P. M. Martin, *Handbook of deposition technologies for films and coatings*, 3rd ed., edited by P. M. Martin (Elsevier, Amsterdam [u.a.], 2010).

[87] S. I. Shah, G. H. Jaffari, E. Yassitepe, and B. Ali, in *Handb. Depos. Technol. Film. Coatings* (Elsevier, 2010) pp. 135–252.

[88] D. Depla, S. Mahieu, and J. Greene, in *Handb. Depos. Technol. Film. Coatings* (Elsevier, 2010) pp. 253–296.

[89] D. M. Mattox, J. Vac. Sci. Technol. A Vacuum, Surfaces, Film. **7**, 1105 (1989).

[90] P. Sigmund, Phys. Rev. **184**, 383 (1969).

[91] J. E. Mahan and A. Vantomme, J. Vac. Sci. Technol. A Vacuum, Surfaces, Film. **15**, 1976 (1997).

[92] Y. Yamamura and H. Tawara, At. Data Nucl. Data Tables **62**, 149 (1996).

[93] T. Ono, T. Kenmotsu, and T. Muramoto, in *Springer Ser. Mater. Sci.*, Vol. 109 (Springer Verlag, 2008) pp. 1–42.

[94] W. D. W. D. Westwood, *Surf. Eng.* (Education Committee, AVS, 2018) pp. 573–581.

[95] S. Mráz, J. Emmerlich, F. Weyand, and J. M. Schneider, J. Phys. D. Appl. Phys. **46**, 135501 (2013).

[96] U. Helmersson, M. Lattemann, J. Bohlmark, A. P. Ehiasarian, and J. T. Gudmundsson, Thin Solid Films **513**, 1 (2006).

[97] O. V. Vozniy, D. Duday, A. Lejars, and T. Wirtz, Plasma Sources Sci. Technol. **20**, 065008 (2011).

[98] D. Lundin, M. Stahl, H. Kersten, and U. Helmersson, J. Phys. D. Appl. Phys. **42**, 185202 (2009).

[99] J. Greene, in *Handb. Depos. Technol. Film. Coatings* (Elsevier, 2010) pp. 554–620.

[100] A. Anders, Thin Solid Films **518**, 4087 (2010).

[101] G. W. H. Höhne, W. F. Hemminger, and H.-J. Flammersheim, *Differential Scanning Calorimetry*, 2nd ed. (Springer Berlin Heidelberg, Berlin, Heidelberg, 2003).

[102] R. Parameshwaran, A. Sarı, N. Jalaiah, and R. Karunakaran, in *Handb. Therm. Anal. Calorim.*, Vol. 6 (Elsevier B.V., 2018) pp. 519–572.

[103] K. Hildal and J. H. Perepezko, in *Handb. Therm. Anal. Calorim.*, Vol. 6 (Elsevier Science B.V., 2018) pp. 781–828.

[104] M. Wagner, *Thermal analysis in practice : fundamental aspects* (2018) pp. 1–349.

[105] Netzsch, "https://www.cif.iastate.edu/sites/default/files/uploads/Other_Inst/TGA/STA449 F1 Operating Instructions.pdf (accessed on 2023-01-18)," (2023).

[106] Netzsch, "https://analyzing-testing.netzsch.com/en/products/simultaneous-thermogravimetry-differential-scanning-calorimetry-sta-tg-dsc/sta-449-f1-jupiter (accessed on 2023-01-18)," (2023).

[107] M. Ermrich and D. Opper, *XRD for the analyst: getting acquainted with the principles* (2011) pp. 1–93.

[108] R. Jenkins and R. L. Snyder, *Introd. to X-ray Powder Diffractometry* (John Wiley & Sons, Inc., Hoboken, NJ, USA, 1996) pp. 1–432.

[109] N. Raval, R. Maheshwari, D. Kalyane, S. R. Youngren-Ortiz, M. B. Chougule, and R. K. Tekade, in *Basic Fundam. Drug Deliv.* (Elsevier, 2019) pp. 369–400.

[110] R. P. Goehner and M. O. Eatough, Powder Diffr. **7**, 2 (1992).

[111] P. Dutta, "Grazing incidence X-ray diffraction," Tech. Rep. 12 (2000).

[112] S. Rißlegger, *Design and construction of an acetylene capable PVD based deposition system* (Diploma Thesis, 2020).

[113] CDL SEC and TU Wien, "https://surface-engineering.tuwien.ac.at/2020/01/13/welcome-frida/ (accessed on 2022-10-06)," (2022).

[114] Plansee, "https://www.plansee.com/de/produkte/titan-diborid-sputtertargets.html (accessed on 2023-01-23)," (2023).

[115] Georg Martin GmbH, "https://pdf.directindustry.de/pdf/georg-martin-gmbh/liefersortiment-m-tech-f-metallfolien-zuschnitte/36564-73251.html (accessed on 2013-01-24)," (2023).

[116] TU Wien, "https://www.tuwien.at/ausstattung/mikroskopie (accessed on 2023-01-24)," (2023).

[117] TU Wien, "https://www.tuwien.at/forschung/facilities/ustem/geraeteausstattung/tecnai-f20 (accessed on 2023-03-04)," (2023).

[118] TU Wien, "https://www.tuwien.at/ustem/geraeteausstattung/fib-scios (accessed on 2023-01-24)," (2023).

[119] TU Wien, "https://www.tuwien.at/forschung/facilities/xrc/ausstattung (accessed on 2023-01-24)," (2023).

[120] V. Moraes, H. Riedl, C. Fuger, P. Polcik, H. Bolvardi, D. Holec, and P. H. Mayrhofer, Sci. Rep. **8** (2018).

[121] L. Silvestroni, G. Meriggi, and D. Sciti, Corros. Sci. **83**, 281 (2014).

Appendix A

Appendix

Table A.1: ICP-OES chemical composition analysis of the DCMS deposited films in the as-deposited state

Thin film	**Target composition**	**Element concentration from ICP - OES**				**B/Me ratio**
	[mol.%]	**Ti** [at.%]	**Mo** [at.%]	**Si** [at.%]	**B** [at.%]	[-]
$Ti_{0.39}Si_{0.04}B_{0.57}$	$TiB_2/TiSi_2$ [90/10]	39.02	-	3.50	57.48	1.47
$Ti_{0.10}Si_{0.35}B_{0.55}$	$TiB_2/TiSi_2$ [80/20]	10.11	-	35.11	54.78	5.42
$Ti_{0.21}Si_{0.13}B^{*}_{0.66}$	$TiB_2/Ti_5Si_3/SiB_6$ [77.12/8.58/14.30]	21.58	-	12.84	65.58	3.04
$Ti_{0.22}Si_{0.13}B^{*}_{0.65}$	$TiB_2/Ti_5Si_3/SiB_6$ [58.89/15.44/25.67]	21.63	-	13.30	65.07	3.01
$Ti_{0.23}Mo_{0.05}Si_{0.11}B_{0.61}$	$TiB_2/MoSi_2$ [85/15]	22.92	4.84	10.63	61.61	2.22
$Ti_{0.33}Mo_{0.06}Si_{0.12}B_{0.49}$	$TiB_2/MoSi_2$ [80/20]	33.48	5.51	12.46	48.55	1.25

* Measured by ICP-MS

Table A.2: ICP-OES chemical composition analysis of as-deposited films sputtered from the TiB_2/$MoSi_2$ [80/20] target with varying bias substrate voltage.

Thin film	**Bias voltage**	**Element concentration from ICP - OES**				**B/Me ratio**
	[V]	**Ti** [at.%]	**Mo** [at.%]	**Si** [at.%]	**B** [at.%]	[-]
$Ti_{0.33}Mo_{0.06}Si_{0.12}B_{0.49}$	-40	33.48	5.51	12.46	48.55	1.25
$Ti_{0.24}Mo_{0.07}Si_{0.12}B_{0.57}$	-80	23.61	7.31	12.21	56.87	1.84
$Ti_{0.24}Mo_{0.06}Si_{0.10}B_{0.59}$	-100	24.23	7.49	9.70	58.57	1.85
$Ti_{0.24}Mo_{0.07}Si_{0.12}B_{0.57}$	-120	24.28	7.27	11.52	56.92	1.80
$Ti_{0.25}Mo_{0.08}Si_{0.07}B_{0.60}$	-150	25.47	7.57	6.54	60.42	1.83

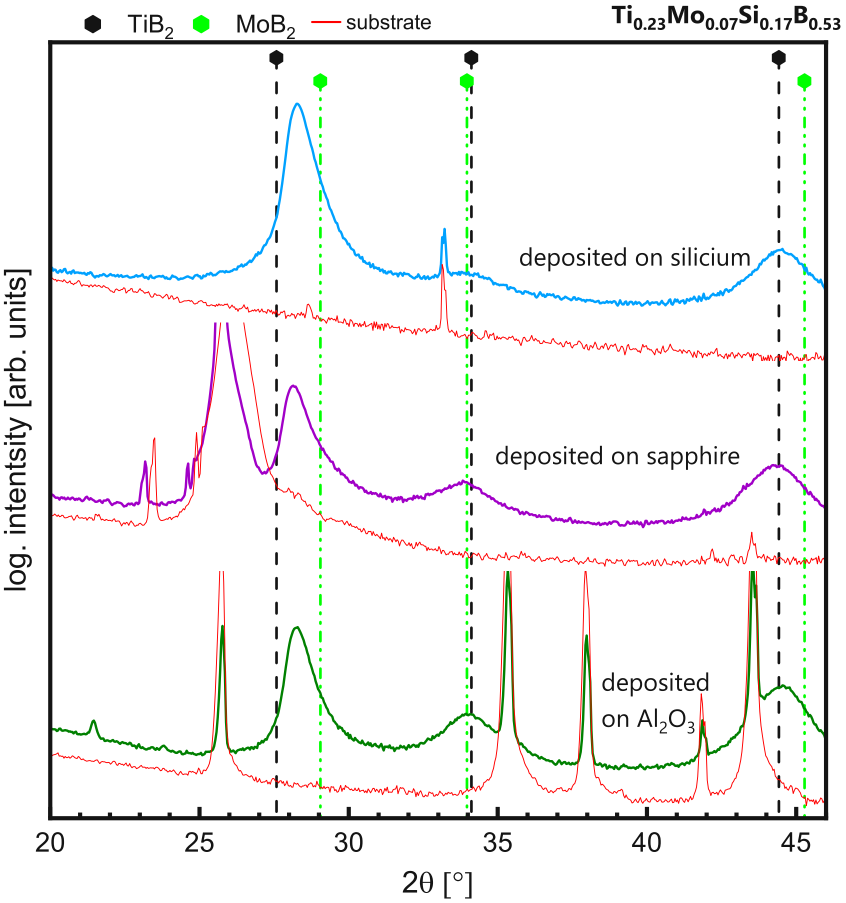

Figure A.1: X-ray diffractograms of the $Ti_{0.23}Mo_{0.07}Si_{0.17}B_{0.53}$ film deposited on various substrates overlapped with scans of the uncoated substrates in red

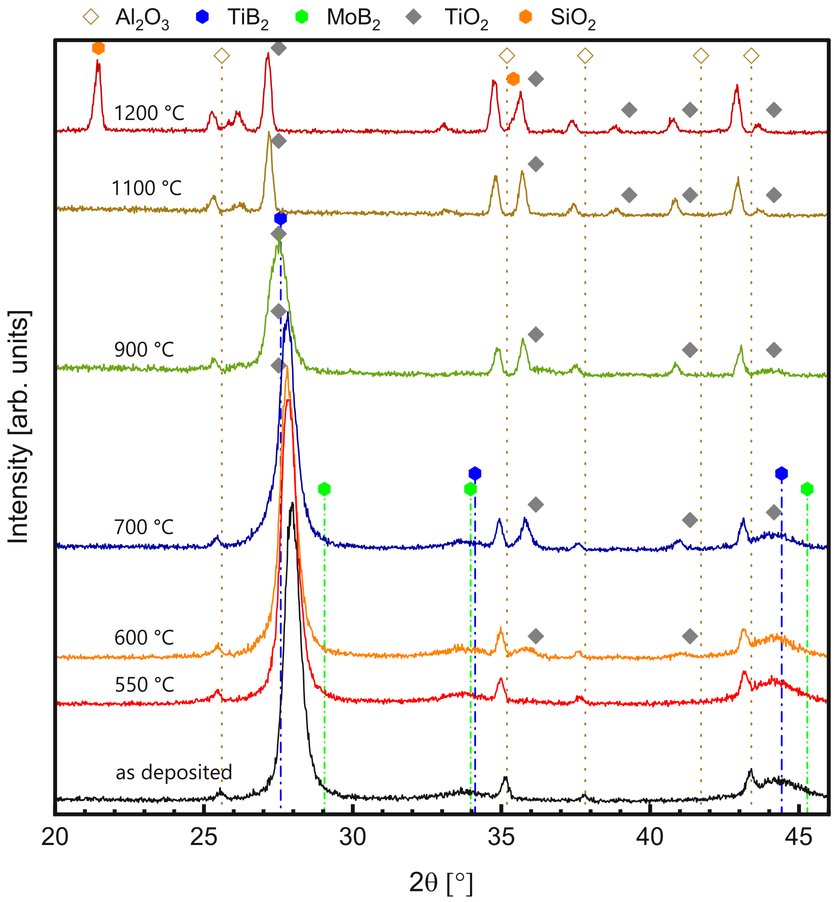

Figure A.2: Grazing incidence in-situ XRD of $Ti_{0.23}Mo_{0.07}Si_{0.17}B_{0.53}$ oxidised in ambient air